# POLITECNICO DI MILANO

SCUOLA DI INGEGNERIA INDUSTRIALE E DELL'INFORMAZIONE
Laurea Magistrale In Ingegneria Meccanica

# SIMULATION-BASED OPTIMIZATION OF ELECTROHYDRODYNAMIC DRYING OF BIOLOGICAL MATERIALS

Supervisor:
Prof. Dr. Paolo Gaetani

Co-Supervisor:
Prof. Dr. Thijs Defraeye

Kamran Iranshahi

Student number: 875817

Academic Year: 2018 - 2019

# ABSTRACT

Electrohydrodynamic (EHD) drying is an effective non-thermal drying technology. Here the dehydration rate of the food product is enhanced by invoking ionic wind via a high voltage difference between the emitter and collector electrodes. Among various conventional emitter-collector configurations used for EHD drying, the wire-to-mesh configuration has recently been found to be promising in terms of drying kinetics, drying uniformity and scalability, compared to the conventional wire-to-plate configuration. This study aims to further enhance the potential of this promising collector design for EHD drying, by providing a next step in improving the collector electrode, to speed up the drying rate and increase. Mechanistic modeling is used to build a more realistic model of the mesh collector than currently used. In the first part, the major driving force for EHD drying are gathered and discussed, as a basis for further model improvements and to get an increased insight in this promising but complex drying technology. In the second part of this computational-theoretical study, the impact of various mesh parameters (wire diameter, wire number and porosity) on the electric field intensity, the resulting Coulomb force on the air flow and the drying rate was explored. To identify tradeoffs between drying rate, energy consumption and fluid mechanic losses, an EHD performance number is introduced. This allows having a comprehensive evaluation of energy efficiency and drying effectiveness of different device designs. In the last part, a more optimal mesh configuration is proposed that improves the overall EHD drying performance number. This improvement was achieved by using a lower number of conducting wires. Their number was chosen in such a way that an intensification of the electric field was obtained, based on an in-depth analysis of the electrostatic conditions. With this optimal configuration, a similar drying rate was obtained, but the resulting energy consumption was reduced with almost a factor 10. This improved mesh collector design is an important step towards EHD drying devices that are scalable to industrial scale, which are sufficiently clean and efficient.

**Keywords:**

Electrohydrodynamic, EHD simulation, multi-phase flow, CFD, dehydration, EHD drying

# ACKNOWLEDGEMENTS

# TABLE OF CONTENTS

## LIST OF FIGURE

# LIST OF TABLE

# Chapter 1: Statement of Purpose

## 1.1 Introduction

Biological materials such as fruits are indispensable sources of essential dietary nutrients, vitamins and minerals. Due to high moisture content (above 80%) they are highly perishable. Losses estimated at 40-50% occur in many developing countries in the tropical and subtropical region due to inadequate refrigeration and freezing facilities (Jayaraman and Das Gupta, 1992). As an alternative to storage of the fresh products, food processing can be used to convert such perishable commodities into stable products that can be stored for extended periods thereby reducing losses and making them available in times of shortage, out of season, and at places far away from the site of production. Processing can also change foods into new or more usable forms and make them more convenient to prepare.

There are various ways of food preservation employed which include canning, freezing, salting, vacuum packing, preserving in syrup, food irradiation and many more. However, dehydration is one of the oldest and most commonly used methods of food preservation (Mujumdar and Jangam, 2011) and it is by far the most useful large scale operation method of keeping solid foods safe for long periods of time, and is of fundamental importance in most sectors of food processing. By definition, food dehydration is the process of removing water from food, to inhibit the growth of enzymes and bacteria. The energy input is often less than what is needed to freeze or can, and the storage space is minimal compared with that needed for canning jars and freeze containers (Ahmed *et al.*, 2013), and the associated transport costs are also reduced.

There are already plenty of conventional dryers with a good performance for drying most materials. However, not all of these drying technologies are necessarily optimal in terms of energy consumption, quality of dried product, safety in operation and minimal environmental impact. Typically, emissions or combustion of large quantities of fossil fuels are required to generate the required thermal energy, which also has a negative environmental impact (Singh *et al.*, 2015) (Kudra and Mujumdar, 2009).

Traditionally, these industrial drying methods are all based on hot air drying by exposing the food to high air temperatures. This exposure results in various compositional/ structural changes, both desirable and undesirable. The use of higher drying temperature produces drastic changes in the physical, chemical, and biological properties of food (Bajgai *et al.*, 2006) (e.g. vitamin C is destroyed by exposure to heat (Ahmed *et al.*, 2013)). Therefore, in some cases using non-

thermal drying technology is vital for heat-sensitive materials such as high-value bioactive components of fruits and medicinal plants (polyphenols, flavonoids, dietary fiber, etc.), living cells (bacteria, yeasts and viruses), and non-living substances of biological origin (blood plasma, serum, hormones, antibiotics, probiotics, nutraceuticals, etc.) (Martynenko *et al.*, 2017). However, non-thermal methods should still guarantee a sufficiently fast drying rate.

Electrically induced processes, such as electroporation, electrocoagulation, electroseparation and electroosmotic drying are widely used in non-thermal food processing (Martynenko and Kudra, 2016a). Among the novel drying methods that have been described in literature so far, electrohydrodynamic (EHD) drying as one of the relatively new methods, has proved to be an effective non-thermal technology in complying with the main issues of conventional dryers such as cost/energy efficiency and product quality (Bajgai *et al.*, 2006; Martynenko and Kudra, 2016b; Defraeye and Martynenko, 2018). Electrohydrodynamics (EHD) is a branch of fluid mechanics concerned with electrical force effects (Melcher and Taylor, 1969) or in other words, interaction of fluids with electric fields (CASTELLANOS, 2008). This phenomenon directly converts electrical energy into kinetic energy without any moveable part and has a variety of possible applications today, including in drying technology (Fylladitakis, Theodoridis and Moronis, 2014). Electrohydrodynamic (EHD) drying refers to the removal of water from a material placed in the strong electric field due to the so-called ''corona wind'' (Kudra and Martynenko, 2015).

The following can be quoted as examples of positive attributes: lower shrinkage, higher rehydration capacity, and preserved nutritional content (e.g. vitamin). Regarding energy consumption, it is claimed to be much lower in both EHD and combined EHD-hot air drying than in simply hot air drying (Kudra and Martynenko, 2015). Compared to mechanically-generated airflow (e.g. a fan), EHD drying has no moving part so it does not induce vibrations and has a shorter response time. There is also more flexibility in the size and geometry of the system, as airflow is produced locally, i.e. below each needle, instead of centrally, as with an axial fan (Defraeye and Martynenko, 2018).

## 1.2 Research Objectives

The majority of the work on EHD drying has been experimental with simple setups (Defraeye and Martynenko, 2018). Although some working prototypes have been built (Lai, 2010), but no commercial EHD dryers are available yet (Defraeye and Martynenko, 2018). Further development and optimization of such devices towards industrial application requires gaining a deep insight about underlying physics of EHD drying. However, in experimental studies of EHD

drying, the product temperatures or (bulk) airflow fields are rarely measured. Advanced laser diagnostics, such as particle image velocimetry, have been used to explore EHD-generated airflow fields (Kocik *et al.*, 2009; Podlinski *et al.*, 2013), but these techniques have not been applied for EHD drying studies yet and also do not provide information about moisture or temperature fields in the air (Defraeye and Martynenko, 2018). Moreover, it is not always possible to measure a quantity over entire domain in an experimental setup. In such cases, numerical modeling and simulation can be used as an alternative to further understand the feasibility and assist in the design and optimization of such a technology (Defraeye, Blocken and Carmeliet, 2011; Halder and Datta, 2012; Defraeye, 2014; Curcio *et al.*, 2016; P, MV and G, 2016). It is a robust tool that can provide an insight into the different physics involved in the EHD drying process, how they interact with each other and how the manipulation of the setup can affect different parameters, in order to improve device design.

In this thesis, the aims is to study emitter-collector design for EHD drying, by providing a next step in improving the collector-electrode configuration, to speed up the drying rate and increase the efficiency of the dryer. Mechanistic modeling is used to build a more realistic model of the mesh collector than currently available model. Numerical modeling of the airflow together with the convective drying process was done using a continuum approach. Such a conjugate modeling strategy provides high spatial and temporal resolution, which enables not only to track the internal moisture distribution, temperature and water activity throughout the entire drying process, but also the heat and moisture transport in the airflow (Halder and Datta, 2012; Curcio *et al.*, 2016; Defraeye and Martynenko, 2018). To the best of our knowledge, before this study in our research group, no simulation-based method was developed which explicitly combines EHD-generated flow with drying of fresh foods, such as fruits or vegetables. Several studies however focused on modeling only EHD flow (Oussalah and Zebboudj, 2006; Ould Ahmedou, Rouaud and Havet, 2009; Saneewong Na Ayuttaya *et al.*, 2012; Fylladitakis, Theodoridis and Moronis, 2014; Ghazanchaei, Adamiak and G.S. Peter Castle, 2015)

This thesis is written in three parts, in the first part of the thesis different EHD drying driving forces associated with their underlying phenomena are studied. Effort has been made to point out the importance of each mechanism. The second part of the thesis deals with the simulation of an electrohydrodynamic drying system. A 2D numerical continuum model is developed that couples EHD-driven airflow to a dehydration model for fruit. Only the most important driving force (characterized from the first part) that is convection is included in the model. In the last part, effort has been made to reach the optimal collector wire

arrangement as a tradeoff between drying time and low energy consumption for industrial application that shows a significant improvement in terms of the performance.

# Chapter 2: Multiphysics Modeling of EHD Drying

The purpose of this chapter is to present a concise introduction to the concepts and governing equations of EHD drying. First, a brief history of EHD and it's general applications will be discussed. Then, the EHD concept and its different sub-processes in EHD drying will be addressed. The base computational model considered in this study is a 2D continuum model composed of a wire as emitter, grounded mesh collector and a rectangular slice (L × H=10×5 mm) of apple fruit as drying material (Fig. 2-1).  By applying a positive high voltage ($V_w$) to the emitter, ionization layer is formed in the vicinity of the emitter. Ions, which are generated at this layer, are accelerated in the drift region due to the electric force ($F_e$), and their movement introduces momentum in the direction of the electric field to the still air and generates EHD driven airflow towards the fruit sample that enhances heat and mass transport in the fruit. In order to model this process, we have to couple 3 different physics of 1-Electrostatics, 2-Airflow and 3-Dehydration in porous media. Hence, in order to review the governing equations and basics it is more convenient to break down the entire process into the mentioned sub-processes.
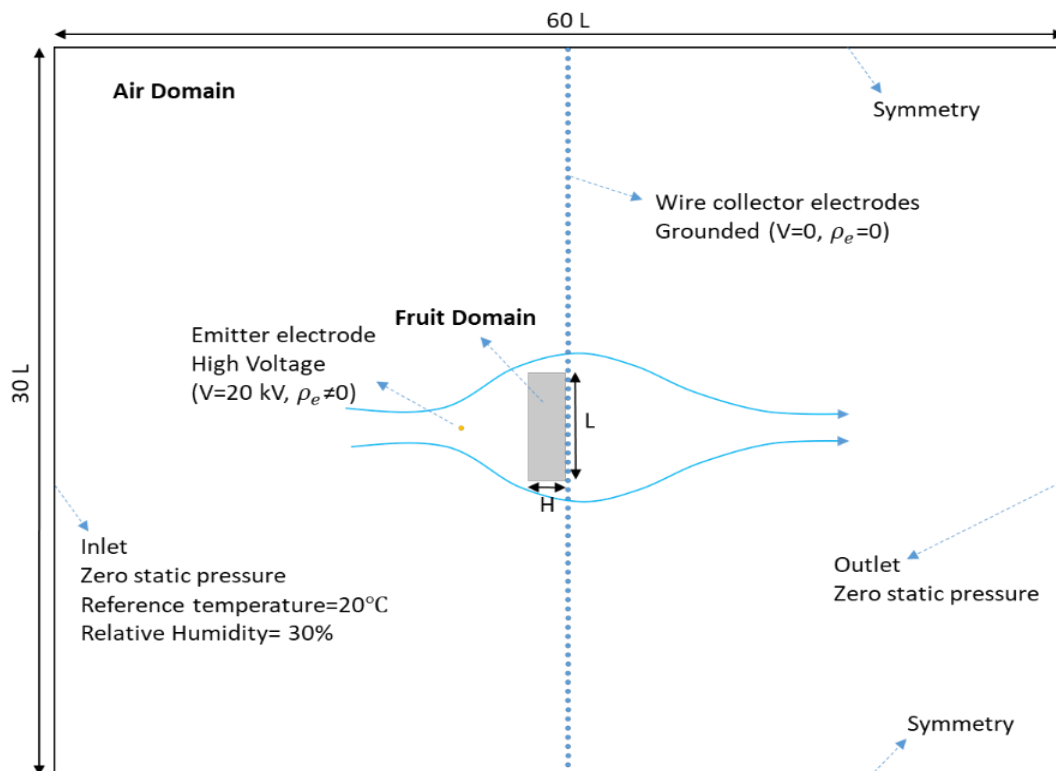


**Fig. 2-1 Computational model and simulation conditions**

## 2.1 Electrohydrodynamics – a brief history

In almost all the EHD-based technologies, a high potential difference between the emitter and collector associated with the large curvature of the emitter locally ionizes the air around the emitter and produces corona discharge. The generated ions, accelerate chiefly by the Coulomb force and modify the airflow structure through the electrohydrodynamic (EHD) effect, in which the movement of charged species towards the grounded collector electrode (corona wind), transfers momentum to neutral air particles through elastic and/or plastic collisions, which ultimately results in a net body force transmitted to the airflow (Fylladitakis, Theodoridis and Moronis, 2014; Iranshahi and Mani, 2018).

The study of Electrohydrodynamics (EHD) is a particular domain of electrodynamics concerned with fluid flow in the presence of electric forces in dielectric media. The dielectric fluid (in this case, dry air) exhibits very low conductivity, thus having the ability to sustain high electric fields with small currents (WAN, 2009).

EHD concepts are relatively mature and have been researched since the 17$^{th}$ century. The earliest observation and recording of electrohydrodynamic effects have been made in 1629 by Niccolo Cabeo, who noticed that sawdust would be attracted toward an electrified body, touch it, and then be repelled (Fylladitakis, Theodoridis and Moronis, 2014). However, he was unable to understand and reveal the physics behind this; thus, the first official acknowledgement regarding the discovery of EHD has been given to Francis Hauksbee (1709), who recorded the first instance of an "ion-wind". He had experienced a weak wind blowing when holding a charge tube close to him (WAN, 2009; Fylladitakis, Theodoridis and Moronis, 2014).

Henceforth, many researches were dedicated to the studies of different applications of "ionic-wind" such as solid-fluid boundary layer modification (Roth, Sherman and Wilkinson, 1998), flow control (Corke *et al.*, 2002), cooling of integrated circuits (Shooshtari, Ohadi and Franca, 2003), electrostatic blower (i.e.,EHD pumping) (Stuetzer, 1960; Johnson and Go, 2017), particulate removal in Electrostatic Precipitators (ESP) (Zhao and Adamiak, 2016), electrostatic ink jet (TA and MA., 1977), Electroacoustics (EHD speakers)(Bastien, 1987), EHD propulsion(CHRISTENSON and MOLLER, 1967) and electrohydrodynamic drying (Barthakur, 1989).

**EHD applications**

- **EHD enhanced heat and mass transfer**
- **EHD pump** (electrostatic blower )
- **Electrospray**: EHD printer, Electrospinning
- **EHD Thruster**: intended to be used as propulsion motors
- **EHD Flow Control**
- **DRYING AND EVAPORATION**
- **Etc.**
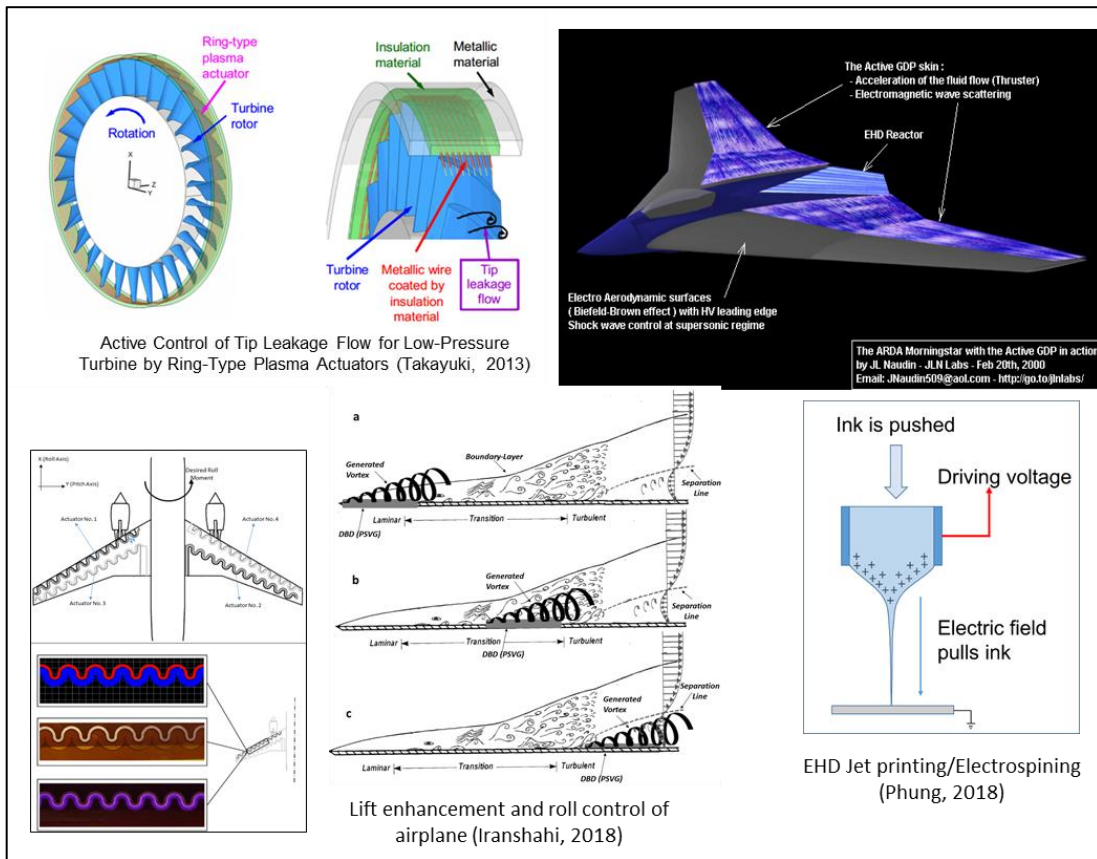


**Fig. 2-2 Different application of EHD (**(Matsunuma and Segawa, 2013; Iranshahi and Mani, 2018; Phung, Oh and Kwon, 2018)**)**

Krueger and his colleagues in 1958 (Krueger, Hicks and Beckett, 1958) were the first ones who reported that the presence of ions in clean air enhances the evaporation rate in water droplets. Since then, especially over the past couple of decades, significant research has been performed over the enhancement of the evaporation rates that EHD could offer (Barthakur and Bhartendu, 1988; Barthakur, 1989; Barthakur and AL‐Kanani, 1990; Fylladitakis, Theodoridis and Moronis, 2014). This application of EHD drew the attention of the agricultural

14

industries when it has been shown that the ionic wind could significantly enhance the dehydration rates of biological materials while it can offer great advantages over heat-based methods and it is a far more energy-efficient method than any form of thermal drying (Chen and Barthakur, 1991; Hashinaga *et al.*, 1999; Cao, Nishiyama and Koide, 2004; Fylladitakis, Theodoridis and Moronis, 2014; Martynenko and Zheng, 2016). Producing less expensive and higher quality biofuels (e.g. rapeseed (Basiry and Esehaghbeygi, 2010)) compared to heat-based drying methods, greatly attract the attention of the energy industries as well (Fylladitakis, Theodoridis and Moronis, 2014).
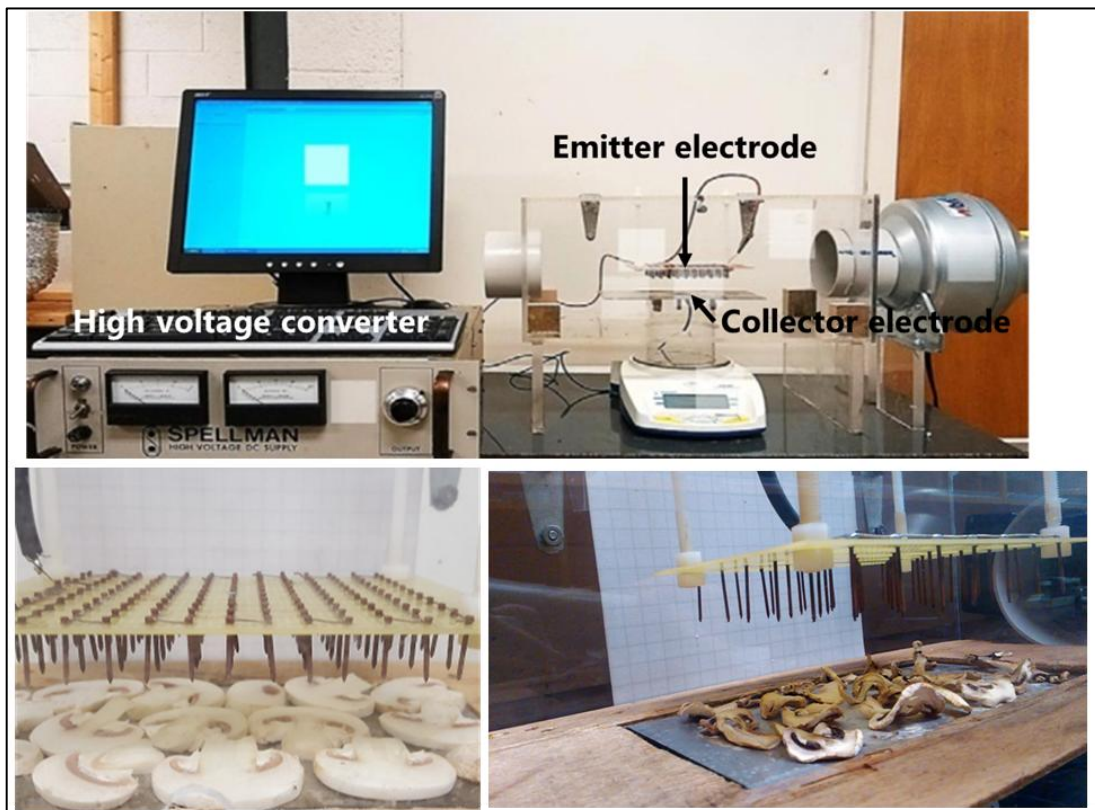


**Fig. 2-3 Typical setup for experimental EHD drying (with courtesy of Alex Martynenko and his research group)**

| Author(s) | Electrode geometry | Drying material | Evaporation rate improvement over ambient air drying |
|---|---|---|---|
| Barthakur and Arnold [100] | Needle-to-Plane | Water | ≈300% |
| Lai et al. [101, 114] | Needle-to-plane | Water | Up to 126% |
| Lai et al. [101, 113] | Wire-to-plane | Water | Up to 240% |
| Alem-Rajabif and Lai [102] | Wire-to-plane | Water | Up to 270% |
| Barthakur and Bhartendu [96] | Needle-to-Plane | Water (100ml) | ≈400% max |
|  |  | Ethyl alcohol (100ml) | ≈250% max |
|  |  | Carbon tetrachloride (100ml) | ≈350% max |
| N.N Barthakur [97] | Needle-to-Plane | Saline water | 210 to 270% (depending on NaCl % concentration) |
| Barthakur and AL-Kanani [98] | Needle-to-Plane | Moisture (soil samples) | 200% to 535% (depending on soil composition) |
| Chen and Barthakur [99] | Needle-to-Plane | Potato slabs | 200% (15 min) |
|  |  |  | 170% (45 min) |
|  |  |  | 140% (180 min) |
| Hashinaga et al. [103] | Needles-to-plane | Apple slices | Up to 120% |
| Bajgai and Hashinaga [104] | Needles-to-plane | Spinach | Up to 300% |
| Cao et al. [105] | Needles-to-plane | Wheat | 50% at 50 °C, 60% at 35 °C, 90% at 20 °C |
| Li et al. [106] | Needle-to-plane | Okara cake | Up to 220% |
| Bajgai and Hashinaga [108] | Needles-to-plane | Radish | Up to 470% |
| Esehaghbeygi and Basiry [109] | Needles-to-plane | Tomato slices | Up to 100% |
| Alemrajabi et al. [110] | Needles-to-plane | Carrot slices | Up to 420% |
| Goodenough et al. [107] | Wire-to-plane | Biscuits | Up to 450% |
| Bai et al. [115] | Needles-to-plane | Scallops | 617% |
| Basiry and Esehaghbeygi [112] | Needles-to-plane | Rapeseed | Up to 275% |
| Isobe et al. [111] | Needle-to-plane | Agar gel | Up to 230% |

**Fig. 2-4 summary of some the research results on EHD-augmented drying (Adopted from** (Fylladitakis, Theodoridis and Moronis, 2014)**)**

## 2.2 EHD drying theory and principle

### 2.2.1 Basic concepts

In EHD drying, a high voltage difference is created between the emitter and collector electrode. Due to the large curvature of the emitter, air is locally ionized, resulting in "corona discharge". The generated ions accelerate towards the grounded collector electrode. Movement of the charged species, transfer momentum to the neutral air particles through elastic and/or plastic collisions and thereby generate an airflow (ionic wind). As such, a net body force is transmitted to the airflow, namely the Coulomb force.
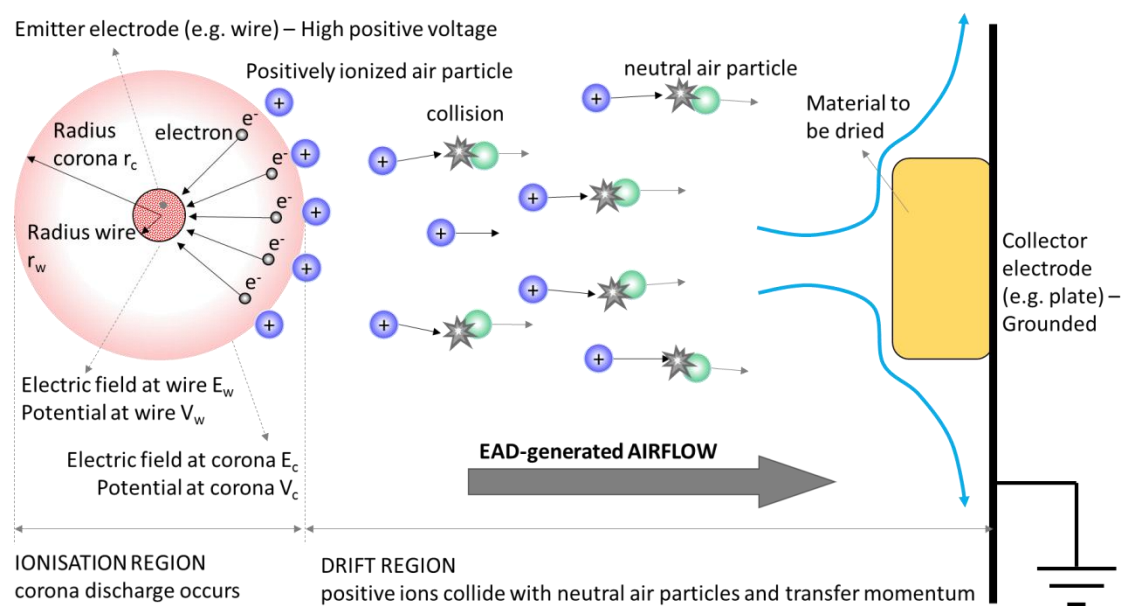


**Fig. 2-5 Schematic illustration of EHD airflow generation process for positive corona discharge (not to scale).**

Electrical discharges generated at atmospheric pressure near sharp points, edges, or thin wires under the action of large electric fields are usually weakly luminous, and referred to as *Corona* (Misra *et al.*, 2018). The primary mechanism for EHD flow generation is the corona discharge (Lai and Lai, 2002). *Corona discharge* refers to the phenomenon when the electric field near a conductor is strong enough to ionize the dielectric surrounding it but not strong enough to cause an electrical breakdown or arcing between conductors or other components (Fylladitakis, Theodoridis and Moronis, 2014). The sharp edges promote the formation of high intensity local electric fields, which results in a decreased breakdown voltage ($V_b$) and helps stabilize the discharge uniformly over the electrode surfaces (Misra *et al.*, 2018). Corona discharges are typically self-sustaining, with the plasma generated being stable and in steady condition for long periods(Misra *et al.*, 2018). This controlled corona discharge can be used

17

to ionize air and induce motion by directly converting the electrical energy into kinetic energy.

The ions generated due to corona discharge are accelerated by the electric force ($F_e$) and move towards the grounded collector electrode. The drift of the ions to the collector and their subsequent friction or collisions with uncharged air molecules (as described by Faraday (Faraday, 1830)) is the reason behind the movement of the air and generation of a so-called corona wind ($\approx 10^{-1}$-$10^1$ m.s$^{-1}$) (Defraeye and Martynenko, 2018).  The principle of EHD drying is based on the use of this ''corona'' wind, also called the ''ionic'' or ''electric'' wind, where electric discharge creates the jet of high-energy ions and gas molecules targeting the dried material (Kudra and Martynenko, 2015). Fig. 2-5 shows a basic graphic representation of the particle stream between two electrodes when high-dc voltage is applied to the emitter.

The emitting electrode is usually a vertical single and multi-needle type or the wire-type placed in parallel to the plate electrode. Although it has been proved that the performance of the needle electrode is better than the wire type when the applied voltage is higher than 15 kV (Lai and Wong, 2003), but the single- and multiple-wire electrodes were studied because they better fit the foreseen industrial units such as ban dryers (Kudra and Martynenko, 2015). Some efforts have been done in order to optimize the impinging corona jets, which mostly includes geometrical optimization for an array of emitter needles in terms of distance between the needles and their configuration(Lai and Wong, 2003; Lai and Sharma, 2005; Martynenko, Kudra and Yue, 2017). Nevertheless, collector elector optimization have been almost neglected that will be a part of the current study.

The amount of the ionized particles or so-called space charge in the drift region is one of the major factor of drying, as it affect the ionic wind generation (Martynenko *et al.*, 2017). It is usually determined as space charge density (SCD) which is the amount of ionized particles in unite volume.

### 2.2.2 Electrostatics and space charge transport modeling

Analyzing the corona discharge physics is very complex. The electric corona discharge itself is a complicated phenomenon to analyze. In the process of the EHD flow generation, the corona discharge's main contribution is to provide the unipolar ions. Therefore, a simplified steady-state unipolar corona model can be used with the assumption that the ionization occurs in a very thin layer with negligible thickness close to the emitting electrode, and charged ions of single polarity are injected into the drift zone (Zhao and Adamiak, 2016).

The governing equations for EHD-driven flow are well established in several works (Oussalah and Zebboudj, 2006; Ould Ahmedou, Rouaud and Havet, 2009; Saneewong Na Ayuttaya *et al.*, 2012; Fylladitakis, Theodoridis and Moronis, 2014; Ghazanchaei, Adamiak and G.S. Peter Castle, 2015; Martynenko and Kudra, 2016a). The electrical potential V [V] is linked to the electric field intensity E [V m$^{-1}$] by Eq.(1). E in air and the fruit is described by Poisson's equation Eq.(2):

$$\boldsymbol{E} = -\nabla V \tag{1}$$

$$\nabla.(\varepsilon_0 \varepsilon_r \boldsymbol{E}) = \rho_e \tag{2}$$

where $\rho_e$ [C m$^{-3}$] is space charge density (SCD) of the ion/fluid medium, $\varepsilon_0$ is the dielectric permittivity of vacuum (8.854×10$^{-12}$ C V$^{-1}$ m$^{-1}$), and $\varepsilon_r$ is the relative permittivity of the material.

The ion transport is described by the continuity equation for current density and the current density in the drift region (Ohm law). The resulting electric current in the drift zone (air) is caused by three phenomena: (1) ions that move from emitter to collector electrode due to the presence of the electric field, where this drift is also called conduction; (2) transport of charged particles due to airflow (advection), (3) diffusion of ions. As such, the electric current density **J** [C m$^{-2}$s$^{-1}$] becomes:

$$\nabla.\boldsymbol{J} = 0 \tag{3}$$

$$\boldsymbol{J} = \mu_e \rho_e \boldsymbol{E} - D_i \nabla \rho_e + \rho_e \boldsymbol{u} \tag{4}$$

Where **J** [C m$^{-2}$ s$^{-1}$] is the electric current density, μ$_c$ is the ion mobility in the air (1.8×10$^{-4}$ m$^2$ V$^{-1}$ s$^{-1}$), D$_i$ [m$^2$ s$^{-1}$] is the diffusivity of the ions and **u** [m s$^{-1}$] is the velocity vector for air. In the particular case of charged particles (i.e. not considering neutral particles), the drift motion produced by the electric field (first term in the equation) is of the order of $\mu_e \rho_e E \sim 10^{-2} - 10^{-1} \, m \, s^{-1}$. This value is much higher than molecular diffusion, $D_i \nabla \rho_e \sim 10^{-5} - 10^{-4}$, or the advection gas motion which is of the order of $\rho_e \mathrm{u} \sim 10^{-4} - 5 \times 10^{-4} \, m \, s^{-1}$. Hence, the drift term is typically dominant, by which the equation reduces to:

$$\boldsymbol{J} = -\mu_e \rho_e \nabla V \tag{5}$$

To solve EHD generated airflow, additional relations are required to specify appropriate boundary conditions for the corona discharge at the emitter electrode. To induce corona discharge, the voltage at the wire is increased until the electric field in the proximity of the wire becomes sufficiently large to induce local breakdown of the air. At this point, a corona with radius $r_c$ is formed (Fig. 2-5) and the critical voltage and electric field are reached at the wire surface ($V_{w,crit}$ and $E_{w,crit}$). The electrical field at the surface of the ionization layer $E_c$ (not

the wire surface) equals the breakdown electric field strength $E_0$, so $E_c = E_0$ at $r_c$ after corona discharge.

A key question is what happens with the corona if the voltage at the wire is increased beyond $V_{w,crit}$. In this regard, Kaptsov's assumption is typically used. It states that if the voltage at the wire is increased beyond $V_{w,crit}$, the electrical field strength on the wire ($E_w$ [V m$^{-1}$]) and the size of the ionization zone (radius $r_c$) remain constant, so:

$$E_w = E_{w,crit}$$
$$r_c = r_{c,crit} \quad \text{if } V_w > V_{w,crit}$$

(6)

This electric field strength at the wire surface $E_w$ under corona discharge can be calculated with Peek's law, which results for a cylindrical wire in (Meroth *et al.*, 1999; Ghazanchaei, Adamiak and G. S Peter Castle, 2015):

$$E_w = E_0 \delta \left( 1 + \frac{0.308}{\sqrt{\delta r_w}} \right)$$

(7)

where $\delta$ equals $T_0 P / T P_0$, with $T_0$ the standard temperature [K], $T$ the actual temperature [K], $P_0$ the standard pressure [Pa] and $P$ the actual pressure of the gas [K]. In this study, $\delta$ is taken equal to 1, which is a good approximation. $E_0$ is taken equal to 3.1 x 10$^6$ V m$^{-1}$ (Goldman and Goldman, 1978; Meroth *et al.*, 1999; Ghazanchaei, Adamiak and G. S Peter Castle, 2015), as used in most studies. Note however that differing values of $E_0$ have been reported by some authors, for example 0.88 x 10$^6$ V m$^{-1}$ (Wan, 2009) or 2.468 x 10$^6$ V m$^{-1}$ (Oussalah and Zebboudj, 2006).

The radius of the corona $r_c$ (ionization region) can be estimated via (Ould Ahmedou and Havet, 2009):

$$E_w r_w = E_c r_c$$

(8)

where $E_c$ equals $E_0$ at the corona surface and $E_w$ can be determined from Eq.(7). This equation can be derived assuming the ion current at $r_w$ and $r_c$ is the same. The voltage at the corona surface can be determined by (Wan, 2009):

$$V_c = V_w - E_w r_w \ln \left( \frac{E_w}{E_c} \right)$$

(9)

With these relations, the electric field at the wire surface during corona discharge $E_w$ can be estimated (at any voltage as it remains constant), as well as the size of the ionization layer $r_c$ and the voltage at the corona surface $V_c$. These are used to specify the boundary conditions in the computational model.

There are however several ways of including the corona discharge at the wire in the computational model:

The ionization region is not explicitly included as a separate zone in the model, and its size is neglected. As such, the drift region is assumed to start directly at the wire surface ($r_w$), which is placed at voltage $V_w$. The required electrical field strength at the wire surface $E_w$ can be estimated with Peek's equation. This is the most commonly applied modelling strategy.

1. The wire and ionization region are not included in the model, but instead the computational model starts at the corona surface ($r_c$, Fig. 2-5), which is at a voltage $V_c$ and at an electric field strength $E_c = E_0$, so equal to the breakdown electric field strength of air. The voltage $V_c$ is calculated by Eq.(9) and the size of the ionization region $r_c$ can be estimated from Eq. (8).

2. The generation of ions in the ionization layer around the wire is explicitly modelled, in addition to the ion transport in the drift region (Tirumala and Go, 2014). This approach of explicitly modelling these two regions was found to be more accurate but more computationally expensive. However, the authors also mention that neglecting the ionization region can be justified if it is small compared to electrode gap.

In this study, we opted for the first approach, but the results are also compared with the second approach.

### 2.2.3 Ionic wind generation modeling

In this part the governing equation for airflow generation due to ion movement will be addressed. (Navier-Stokes equations). The impact of the electric field on the fluid flow is represented by including a volumetric source term Fe [kg m$^{-2}$ s$^{-2}$] in the momentum equation while it obtains its value from electrostatic variables. This force is the link between the airflow and the electrostatic physics.

$$\rho_a \frac{\partial}{\partial t}(u) + \rho_a (u \cdot \nabla)u = -\nabla p + \mu_a \nabla^2 u + \rho_a g + F_E \tag{10}$$

$$F_E = \rho_c \vec{E} - \frac{1}{2}\varepsilon_0 |E|^2 \nabla \varepsilon + \frac{1}{2}\varepsilon_0 \nabla \left( |E|^2 \rho_a \frac{\partial \varepsilon}{\partial \rho_a} \right) \tag{11}$$

Where $\rho_a$ is the air density (1.20 kg m$^{-3}$ at 20 °C), $\mu_a$ is the dynamic viscosity of air (1.81 × 10$^{-5}$ kg m$^{-1}$s$^{-1}$ at 20°C), and ε is the relative dielectric permittivity of the gaseous medium.

This electric force consists of three parts. In particular, the first term represents the Coulomb force, the second term is known as Dielectrophoretic force, and the third term is Electrorestrictive force. The Dielectrophoretic and Electrorestrictive forces are only of significance if an alternating electric field (or inhomogeneous dielectric media) is applied with a period much shorter than the charge relaxation time and/or the ionic transit time (Shrimpton, 2009). Consequently, Ion movements in the gaseous media and in the absence of a two-phase interface and/or alternating electric field imply that the second and the third terms have a negligible effect on the flow field (Martynenko and Kudra, 2016a), therefore usually only Coulomb force is considered as electric force in most studies:

$$F_E = \rho_c \vec{E} = -\rho_c \nabla V \tag{12}$$

## 2.2.4 Dehydration of fruit tissue modeling

The mass transfer enhancement under EHD effect could be attributed to several driving mechanisms such as ionized convective flow, free energy variation due to the strong electric field, double electric layer, electrical charge barrier and etc. In the current model, only convective dehydration mechanism is considered in such a way that the convective heat and mass transfer coefficients (CHTC and CMTC) are determined from flow field calculations and are employed for fruit dehydration rate calculations.

To calculate heat and moisture (mass) transfer inside the fruit tissue during drying, a previously developed model is used (Defraeye and Verboven, 2017), so only the main characteristics are highlighted here. The main model assumptions are that evaporation is assumed to occur only at the tissue surface and that shrinking and swelling of the tissue are neglected as often assumed in multiphysics modeling of fruit drying (Defraeye, 2014).

### 2.2.4.1 Conservation equations

The following conservation equations for moisture and energy are solved to the dependent variables temperature $T$ [K] and water potential $\psi$ [Pa]:

$$\frac{\partial w_m}{\partial \psi} \frac{\partial \psi}{\partial t} + \nabla \cdot (-K_m \nabla \psi) = 0 \tag{13}$$

$$h_l \frac{\partial w_m}{\partial \psi} \frac{\partial \psi}{\partial t} + \left(c_{p,s} w_s + c_{p,l} w_m\right) \frac{\partial T}{\partial t} + \nabla \cdot \left(-h_l K_m \nabla \psi\right) + \nabla \cdot \left(-\lambda_{PM} \nabla T\right) = 0 \tag{14}$$

where $w_s$ is the dry matter density (solid, 130 kg m$^{-3}$) and $w_m$ is the moisture content of the tissue [kg m$^{-3}$]. $K_m$ is the moisture permeability of the tissue (8 x

$10^{-16}$ s), $h_l$ is the enthalpy of liquid water [J kg$^{-1}$], $\lambda_{PM}$ is the thermal conductivity of the tissue (porous medium, 0.418 W m$^{-1}$ K$^{-1}$), $c_{p,s}$ and $c_{p,l}$ are the specific heat capacities of dry matter (1634 J kg$^{-1}$ K$^{-1}$) and liquid water (4182 J kg$^{-1}$ K$^{-1}$), respectively. For $K_m$ and the sorption isotherm, the values for the apple cultivar *Braeburn* are taken (Aregawi *et al.*, 2013).

### 2.2.4.2 Constitutive equations

The enthalpies of liquid water and water vapor, $h_l$ and $h_v$ [J kg$^{-1}$], are:

$$h_l = c_{p,l}\left(T - T_{ref,0}\right) \tag{15}$$

$$h_v = c_{p,v}\left(T - T_{ref,0}\right) + L_v \tag{16}$$

where $L_v$ is the heat of vaporization (2.5 x 10$^6$ J kg$^{-1}$), also called latent heat, which is the energy needed for the phase change from liquid to vapor. $T_{ref,0}$ is a reference temperature, taken equal to 273.15 K (0°C) and $c_{p,v}$ is the specific heat capacity of water vapor (1880 J kg$^{-1}$K$^{-1}$). To determine the moisture capacity

$$C_m = \frac{\partial w_m}{\partial \psi}$$

the sorption isotherm ($w_m$ vs. water activity $a_w$) is required, as well as the relation of the water activity $a_w$ to the water potential $\psi$. The latter is given by:

$$\psi = \rho_l R_v T \ln\left(a_w\right) \tag{17}$$

where $\rho_l$ is the density liquid water (1000 kg m$^{-3}$) and $R_v$ is the specific gas constant for water vapor (461.52 J kg$^{-1}$K$^{-1}$). The sorption isotherm equals:

$$w_m\left(a_w\right) = w_s \left(\frac{0.15926}{\ln\left(\dfrac{1.0177}{a_w}\right)}\right)^{\frac{1}{0.97014}} \tag{18}$$

### 2.3 Boundary and initial conditions for the simulation

To obtain EHD-generated airflow the equations introduced in previous sections are solved with appropriate boundary conditions which were applied on the fruit surface. Note that, the potential field (Eq. (2)) is also solved inside the fruit. The Navier-Stokes equations for turbulent flow are solved by applying the Reynolds-averaged Navier-Stokes (RANS) approach in combination with the standard k-ε turbulence model. This turbulence model is still the most commonly used model

in computational fluid dynamics (CFD) engineering (Casey and Wintergerste, 2000). Wall functions are used to model transport in the boundary layer. The grid resolution in the boundary layer region was made sufficiently dense to have very low values of the dimensionless wall distance ($y^+$ value). The $y^+$ values were typically below 5 on the fruit surface. At these low $y^+$ values, the boundary layer is actually fully resolved down to the viscous sublayer, by which it corresponds to low-Reynolds number modeling (Defraeye, Blocken and Carmeliet, 2010; Defraeye, Verboven and Nicolai, 2013). Buoyancy effects are not taken into account in the simulations. Long-wave radiation exchange between fruit and the surrounding surfaces is also not included. To solve EHD generated airflow, additional relations are required to specify appropriate boundary conditions for the corona discharge at the emitter electrode. These relations are given in the Supplementary Material.

### 2.3.1 Electrostatics and space charge density

The boundary conditions for electric potential are a high voltage at the emitter (wire) $V_w$, a grounded collector electrode ($V_{col} = 0$ V) and a zero-flux condition on all other boundaries. The electrical potential at the fruit surface results from the calculation as it is an internal boundary. However, the much larger relative permittivity of the fruit $\varepsilon_r$ tissue, compared to that of the air (54 vs 1), makes that the electric potential at the fruit surface was quite low ($V_{fs} \sim 10^2$ V in this study for the base case), for the case where the fruit is placed on the collector surface. A constant relative permittivity used in this study, due to lack of more detailed data.

The boundary conditions for space charge density (SCD) are a specified SCD at the emitter $\rho_{e,w}$, a zero SCD at the collector, and fruit surface and a zero-flux condition on all other boundaries. The SCD at the emitter $\rho_{e,w}$ should be specified in such a way that it leads to electric breakdown at the corona surface. This implies that $E_w$ attains the value calculated by Eq.(7) at some location on the emitter. After this value is attained, the electric field remains constant with increasing voltage, according to Kaptsov's assumption. To this end, the SCD is determined iteratively in such a way that the resulting maximal electric field strength at the emitter surface becomes equal to $E_w$, calculated by Eq.(7).

### 2.3.2 Airflow

The EHD effect will induce airflow from the emitter electrode to the collector electrode, so towards the fruit, due to the ion movement. This will draw air from the inlet into the domain, which will exit at the outlet. At both inlet and outlet of the computational domain, a zero static pressure is imposed. For the air entering the domain, the turbulence intensity was about 1%. For configurations where air

flows around the fruit, the lateral boundaries are modeled as slip-wall boundaries (symmetry), which assume that the normal velocity component and the normal gradients at the boundary are zero. The interface of the air with the fruit and also the emitter (wire) and collector electrode surfaces are modeled as no-slip boundaries for momentum transport.

As mentioned, also convective heat transfer from the fruit surface is modelled to determine the convective heat transfer coefficient (CHTC) distribution on the fruit surface. This CHTC info will be used to specify the boundary conditions for the subsequent dehydration simulation. To this end, a temperature difference of 10 °C was set between the fruit surface $T_{fs}$ and the air which enters the domain at the inlet ($T_{ref}$). The choice of this temperature difference is arbitrary as it is only required to determine the CHTC on the fruit surface. All other boundaries are set to adiabatic. The CHTC distribution over the fruit surface ($h_{c,T}$ [W m$^{-2}$ K$^{-1}$]) can then be calculated from this temperature difference and the local convective heat flux at the air-fruit interface ($g_{c,T}$ [J m$^{-2}$ s$^{-1}$]):

$$g_{c,T} = h_{c,T}\left(T_{fs} - T_{ref}\right)$$  (19)

### 2.3.3 Fruit dehydration

As drying is a transient process, initial conditions are required. The apple fruit is assumed to be initially in fresh-cut state with uniform moisture content $w_{m,ini}$ of 780 kg m$^{-3}$ at a uniform temperature $T_{ini}$ of 20°C. This moisture content leads to a dry-base moisture ratio $X_{ini}$ of 6 (= $w_{m,ini}/w_s$ [kg kg$_{dm}^{-1}$]).

To calculate the convective exchange of the fruit with the environment due to airflow, the convective transfer coefficients (CTCs) for heat and mass on the fruit surface are imposed. To this end, the convective heat transfer coefficient distribution on the fruit surface is derived a-priori from the airflow calculation, as detailed above (Eq. (19)). Only the CHTC is calculated using this "the semi-conjugate" approach. The convective mass transfer coefficient (CMTC) is estimated from the CHTC using the heat and mass transfer analogy, similar as in (Defraeye, Blocken and Carmeliet, 2012). The corresponding CMTC/CHTC ratio (analogy factor) is 7.03 x 10$^{-9}$.

Using these CTCs, the fruit is dried with airflow entering from the inlet at a constant temperature ($T_{ref}$) of 20°C and relative humidity ($RH_{ref}$) of 30 %. To this end, following boundary conditions are specified at the air-fruit tissue interface (continuity of fluxes):

$$\mathbf{n}\cdot\left(-K_m\nabla\psi\right) = g_m = h_{c,m}\left(p_{v,fs} - p_{v,ref}\right)$$  (20)

$$\mathbf{n} \cdot \left( -h_l K_m \nabla \psi - \lambda_{PM} \nabla T \right) = g_T = \left( h_{c,T} \left( T_{fs} - T_{ref} \right) - h_v g_m \right) \tag{21}$$

where $g_m$ [kg m$^{-2}$ s$^{-1}$] and $g_T$ [J m$^{-2}$ s$^{-1}$] are the mass and heat fluxes at the interface, $\mathbf{n}$ is the unit vector normal to the interface, $h_{c,m}$ is the convective mass transfer coefficient (CMTC [s m$^{-1}$]), $h_{c,T}$ is the convective heat transfer coefficient (CHTC [W m$^{-2}$ K$^{-1}$]), $p_{v,fs}$ and $p_{v,ref}$ are the vapor pressures at the fruit surface and of the ambient air [Pa].

The vapor pressures $p_{v,fs}$ and $p_{v,ref}$ are determined based on the water activity at the interface ($a_{w,fs}$) and the relative humidity of the approach air during drying ($RH_{ref}$), via the saturated vapor pressure ($p_{v,sat}$ [Pa]) at the corresponding temperatures:

$$p_{v,fs} = a_{w,fs} p_{v,\mathrm{sat}} \left( T_{fs} \right) \tag{22}$$

$$p_{v,\mathrm{ref}} = RH_{ref} \, p_{v,\mathrm{sat}} \left( T_{ref} \right) \tag{23}$$

$$p_{v,\mathrm{sat}} \left( T \right) = e^{65.8094 - \frac{7066.27}{T} - 5.976 \ln T} \tag{24}$$

For heat transfer, the boundary condition states that heat loss from the fruit tissue due to conduction and liquid water transport equals the convective (sensible) heat exchange with the environment and the heat removal due to the water vapor loss, including evaporation. For mass transfer, the boundary condition states that the moisture loss from the fruit tissue equals the convective vapor removal from the surface.

## 2.4 Computational model

Convective EHD drying of fruit is modeled using the finite-element method. The computational model in this study is a 2D continuum geometry, composed of a wire as the emitter electrode, a grounded mesh as the collector electrode and a rectangular slice of apple fruit (L × H=10×5 mm) as the material that is dehydrated (Fig. 2-6). The EHD generated airflow draws dry air at a temperature $T_{ref}$ of 20°C and a relative humidity $RH_{ref}$ of 30% from the inlet towards the fruit to be dried. These are typical conditions for convective drying of fruit in the ambient environment. Mesh sensitivity analysis was also carried out to ensure that appropriate grids were built for the air and fruit domains. Two groups of configurations are simulated in order to deal with the two major goals of this study. In all of these configurations, emitter–collector distance and the voltage at emitter wire are considered as 20 mm and 20 kV respectively. Other simulation

conditions, as well as the computational model and a summary of coupled equations are summarized in Fig. 2-6.
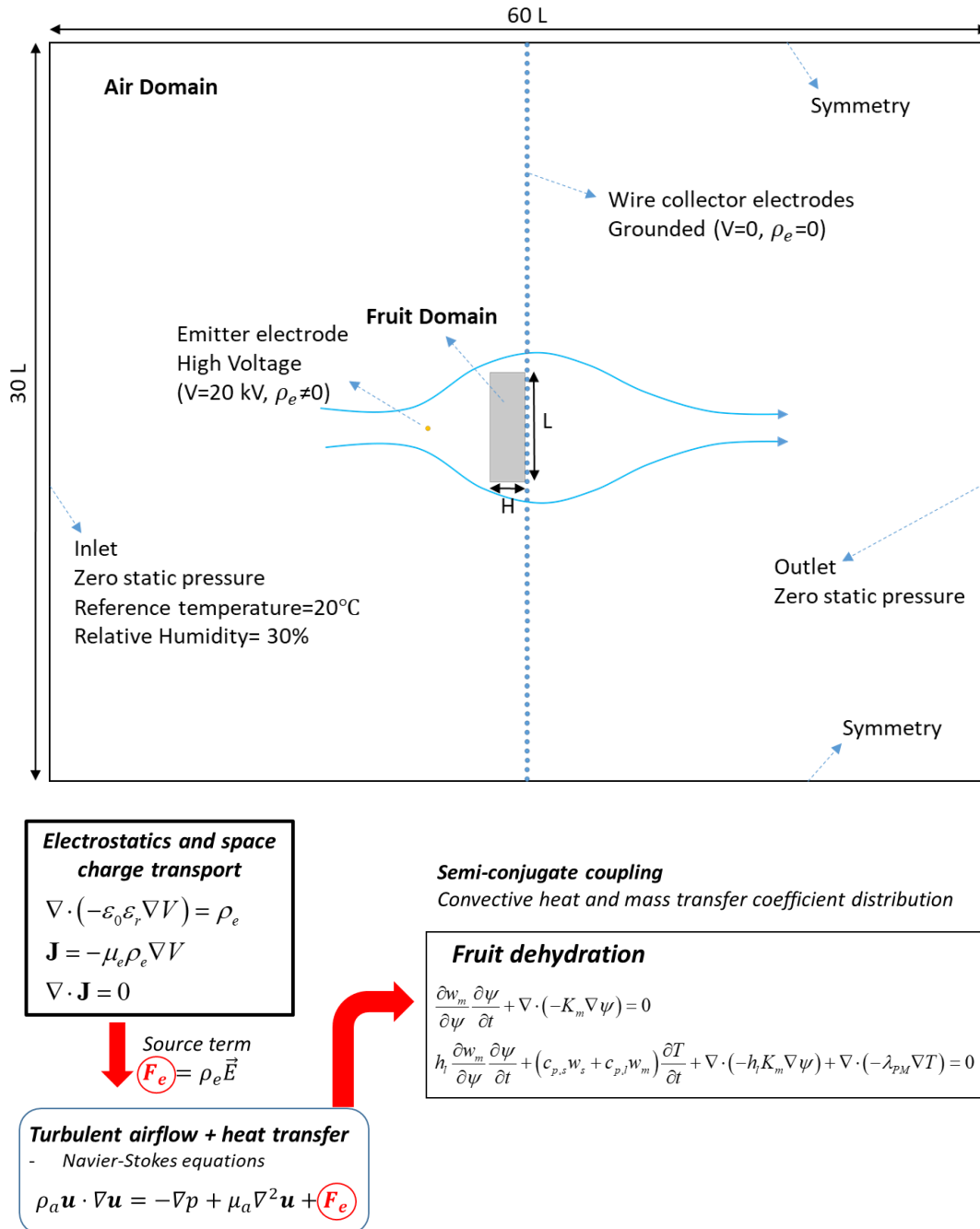


**Fig. 2-6 Computational model, simulation conditions and coupling equations**

## 2.5 Numerical simulations

This model is implemented in COMSOL Multiphysics (version 5.4a). Firstly, in order to obtain the critical SCD value on emitter surface for corona formation, a parametric sweep was performed and the average of resulting values based on

different criteria (e.g. (Jewell-Larsen *et al.*, 2008; Ongkodjojo Ong, Abramson and Tien, 2014)) has been selected. Having this correct SCD, the electrical potential and space charge density distribution at the same time were solved as stationary problems. Then the turbulent airflow and the transient dehydration process were solved sequentially. The convergence threshold and other solver settings were determined based on sensitivity analysis in such a way that increasing the tolerance further did not alter the solution results anymore. After the airflow became stationary, the mass and heat transfer coefficients on the fruit surface were obtained and applied to fruit boundaries. Drying process for 25 h was simulated, starting from the specified initial conditions.

## 2.6 Metrics to evaluate drying performance

The drying performance evaluation and comparison are based on the critical drying time, by which only one drying value is obtained per drying curve. Critical drying time ($t_{crit}$) is defined as the time needed for the sample to reach the critical moisture content ($w_{crit}$). The critical moisture content is considered as 37.8 kg m$^{-3}$ for this study. It is defined as the averaged moisture content in the sample that corresponds to an equilibrium water activity below which no spoilage occurs (Defraeye and Verboven, 2017). Using $t_{crit}$ gives us the opportunity to have a simple quantitative way to compare different drying curves with only one single value.

Although the critical drying time is a good parameter to evaluate different drying performances but it is not sufficient to compare whole the process including energy consumption and losses. Therefore, in order to have an overall evaluation of an EHD drying device, a thorough index is needed. To the best of our knowledge, there is not such an index available for EHD drying devices, so far. Thus, getting inspiration of the effectiveness index defined for EHD flow control devices (Kriegseis *et al.*, 2013; Iranshahi and Mani, 2018), an index but for EHD drying devices is defined below.

Considering all the operating parameters and different processes occur in EHD based devices mentioned previously, overall three performance indicators should be defined for the three main stages of the entire process. Electrical efficiency $\eta_E$, that takes into account the corona (plasma) generation losses and it is defined as the power delivered by the energy source ($P_i = V \times I$) to the discharged power of the emitter ($P_e = \mathbf{J} \times \mathbf{E}$):

$$\eta_E = \frac{P_e}{P_i} \tag{25}$$

In this study, for the calculation of $P_i$, V is constant and has been set equal to 20kV and for I Eq.(55) has been used while $P_e$ is calculated from Eq.**Error! Reference source not found.**.

$$P_e = \oiint_{domain} \vec{E}.\vec{J}d\vec{s}$$  (26)

In the next step, it is desired to see how much of the power which is given to the ions by the emitter, is turned to the air momentum. Here is the place to take into account the losses due to plastic collisions, ion dissipation, thermal radiation, sound/light emission and all the other losses associated with energy transfer from accelerated charged particles to the airflow. This efficiency index, known as fluid mechanic efficiency, can be defined as follow:

$$\eta_{FM} = \frac{P_f}{P_e}$$  (27)

Where $P_f$ is flow power and as it is defined for the pumps $P_f = \dot{m}\,w$ where $\dot{m}$ [Kg s$^{-1}$] is flow rate and w [Nm kg$^{-1}$] is specific work. This equation can be simplified as $P_f = Q(\Delta P)$ where $\Delta P$ is pressure difference generated between emitter and collector. In a more general way, $P_f = \oiint \vec{V}.\nabla P ds$, where Q is volumetric flow rate. Note that, because it is difficult to calculate this power index in practice, usually it is substituted by thrust force ($F_T$), that is more straight forward to be calculated in field. Then $\eta_{FM}$ will change into $\eta_{FM}^*$ which is a dimensioned value [N W$^{-1}$] and it is not an efficiency index anymore so it is called fluid mechanic effectiveness. It is noteworthy to mention that due to the high amount of losses in this sub-process, the value obtained for this parameter is very small so it is more common to use [mN W$^{-1}$] instead of [N W$^{-1}$].

Now it is time to consider the impact of drying performance in the overall performance of the device. Critical drying time is a powerful tool for this purpose and to make it non-dimensional and comparable with other drying technologies, a reference critical drying time should be selected. However, because this overall effectiveness index is defined only for EHD drying technology, it is more straightforward to neglect reference critical drying time. Accordingly, the drying performance indicator can be defined as;

$$\eta_{drying}^* = \frac{1}{t_{crit}}$$  (28)

Which is not an efficiency index as it can be higher than 1 and it is a dimensioned value, so it is called drying effectiveness. The multiplication of these three efficiency/effectiveness indices results in a number that here in after it is called

EHD performance number (Eq. (29)). The higher the EHD performance number, the better the device in terms of energy efficiency and drying effectiveness.

$$\eta^*_{EHD\_Drying} = \eta_E \eta_{FM} \eta^*_{drying} \tag{29}$$

The terms efficiency and effectiveness are used loosely here that may need some elaboration to clarify the distinction between them. Effectiveness measures how adequate the EHD device accomplishes its purposes. One of the major purposes is low drying time. Hence, in this paper effectiveness mostly refers to drying time. An EHD device is more efficient if it consumes lower energy and contains lower losses. However, an efficient EHD drying device can remain efficient while its effectiveness is low or vice versa. Therefore, these two terms have been precisely distinguished in this paper.

The energy consumption calculation in this study has been done based on multiplying of input power ($P_i$) and critical drying time ($t_{crit}$). In order to make it more general and sensible, the consumed energy [MJ] is defined per fresh fruit weight [kg] and it is called specific energy consumption [MJ kg$^{-1}$].

It should be noted that the term "region of interest" is used in this paper to describe a region close to the sample in which the most variation and largest gradients occur there. Therefore, probably the phenomena that play important roles in convective drying and are needed to be captured, take place in that region. For this study, a rectangle with a width of 10 sample length ($L_s$) and a length of 5 $L_s$ around the sample, is considered as the region of interest. This specific area includes the sample, the emitter and a part of the mesh collector close to the sample.

# Chapter 3: Major driving forces in EHD drying

## 3.1 Introduction

Moisture removal from the product in EHD drying could be attributed to various physical phenomena (Martynenko *et al.*, 2017). Extensive research has been done on EHD drying the past two decades, which illustrated the enhancement in terms of drying rate and product quality ((Bajgai *et al.*, 2006; Martynenko and Kudra, 2016b; Defraeye and Martynenko, 2019)). However, not a lot of attention has been paid to why exactly such improvements in drying rate are obtained. Hence, there is still a lack of knowledge on the actual driving mechanisms of moisture removal during EHD drying. To the best of our knowledge, there is no comprehensive study available that analyses all the existing drivers and quantifies their relative impact on dehydration rate. This is the aim of this chapter. To this end, an extensive literature review has been done and analytical calculations have been performed as a first step to quantify different contributions.

The driving forces in EHD drying can be divided into three groups based on their main region of action, namely in the air domain, at the air-material interface, and in the material itself. This categorization is shown in **Error! Reference source n ot found.**. In this figure, the green boxes are the region of action, the blue boxes are the driving forces and the red boxes are related to underlying phenomena. In the following paragraphs, different driving forces will be studied based on this categorization.
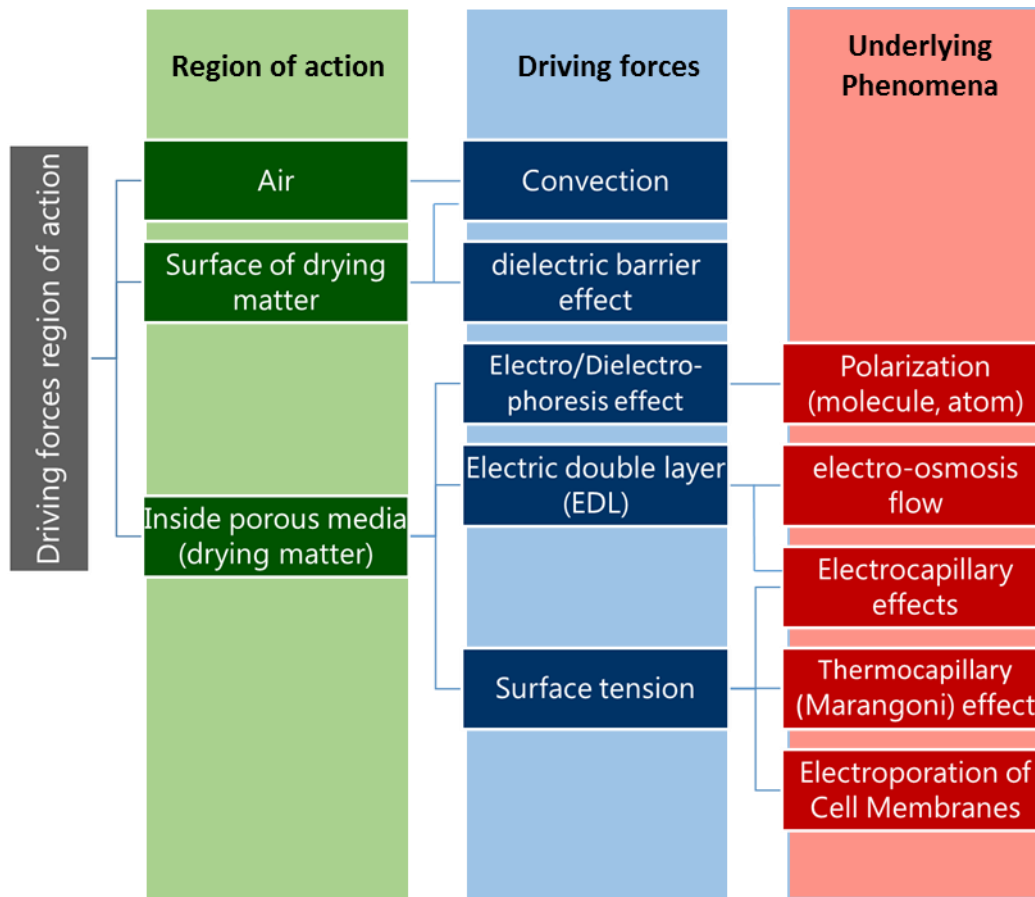
**Fig. 3-1 Driving force classification based on region of main action and origination**

## 3.2 Region of action: Air

### 3.2.1 Convection

Convection is one of the heat and mass transfer mechanisms that is due to the bulk movement of molecules within fluids such as gases and liquids. Some studies (e.g. (Kibler and Carter, 1974; Alem-Rajabif and Lai, 2005)) found that the evaporation rate enhancement is due to the reducing evaporation front in solid-gas interface (the material surface). Especially, (Kibler and Carter, 1974) states it appears to be no reason to assume that the electrocooling process involves any mechanism other than electrically induced forced convection. Moreover, (Martynenko *et al.*, 2017) concluded that EHD drying is convective in nature, associated with additional mass transfer due to ionic wind. Although the other reported results show something more than only convection, but such mentioned conclusions indicates the importance of convection mechanism in drying. In the following paragraphs analytical calculation for ionic wind dehydration is presented.

32

The equation for convection mass transfer can be derived from mass conservation law by applying Type 3 boundary condition (Robin)(Martynenko *et al.*, 2017). This links water diffusion to the material surface and convection from the material surface:

$$\frac{dm}{dt} = D\frac{\Delta m}{\Delta x} = h_m(m - m_\infty) \tag{30}$$

Where D is the water diffusivity [m$^2$ s$^{-1}$], x being the material thickness [m], m$_\infty$ vapor concentration of ambient gas [kg m$^{-3}$] and h$_m$ stands for the mass transfer coefficient [m s$^{-1}$]. Now the aim is to link h$_m$ to the ionic wind.

From the momentum conservation law, it is possible to estimate the ionic wind velocity. The momentum equation can be considered as (31), where $\rho$ is density of the air, $u$ is velocity vector, $\tau$ the vectorial shear stress and $P$ is pressure.

$$\rho\frac{Du}{Dt} = -\Delta.\tau - \Delta P + \rho g \tag{31}$$

The ion-drag force is defined in literature ((Robinson, 1961; Mujumdar and Mashelkar, 2013)) as

$$\nabla P = \rho_e E \tag{32}$$

Where $\rho_e$ is space charge density [C m$^{-3}$] and E is electric field intensity [V].

By inserting (32) into (31) and some simplification, the ionic wind velocity from the electric field force at the surface of the collecting electrode can be estimated as follows(Martynenko *et al.*, 2017):

$$\frac{\rho u_e^2}{2} = \int_0^d \rho_e E dz \tag{33}$$

By considering uniform or non-uniform E, equations (34) and (35) can be derived, respectively.

$$u_e = \sqrt{\frac{\varepsilon_0}{\rho}}E \tag{34}$$

$$u_e = \sqrt{\frac{jd}{\rho\mu}} \tag{35}$$

with
$$j = j_0 \cos^5\theta$$

Where $\varepsilon_o$ represents dielectric permittivity of vacuum [8.85 pF/m], d is emitter-collector distance, $\mu$ is ionic mobility, $j_0$ is the maximum current density (just underneath the emitter) and $\theta$ is Warburg angle.
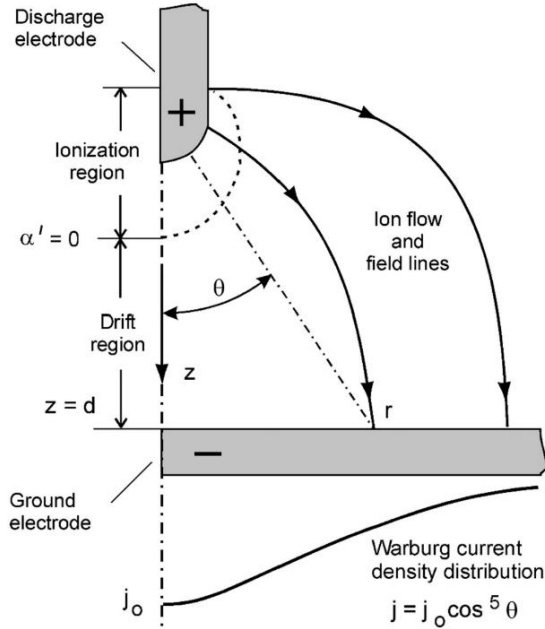


**Fig. 3-2 typical pin-to-plane corona geometry and Warburg angle determination (Adopted from (Goldman & Goldman 1978))**

(Kibler and Carter, 1974) defines a formulation for a reasonable value of average ionic wind velocity on the surface of the collector,

$$\bar{u}_e = [\left(\frac{2d}{A}\right)\left(\frac{i}{\mu\rho}\right)]^{\frac{1}{2}} \tag{36}$$

where A is the collector surface area and *i* is the total current leaving the emitter (corona current). On the other hand, forced convection heat transfer coefficient for a circular plate exposed to uniform air velocity of $\bar{u}$, is defined as (Kibler and Carter, 1974):

$$h_{T\bar{u}} = (\frac{k_f}{\pi^{\frac{1}{4}}})(\frac{\bar{u}}{\nu D})^{\frac{1}{2}} \tag{37}$$

where $k_f$ is the thermal conductivity of the surface film, $\nu$ is the kinematic viscosity, and D is the plate diameter. So by inserting (36) into (37), we can estimate the convective heat transfer coefficient due to ionic wind. The same methodology can be applied for mass transfer coefficient. So the convective mass transfer coefficient will be as follow:

$$h_{m_{\overline{u}_e}} = (\frac{2k_f}{D(\pi v)^{\frac{1}{2}}})(\frac{2di}{\mu\rho})^{\frac{1}{4}} \tag{38}$$

Finally, the evaporation rate can be considered as:

$$(\frac{dm}{dt})_c = h_{m_{\overline{u}_e}}(m - m_\infty) = (\frac{2k_f}{D(\pi v)^{\frac{1}{2}}})(\frac{2di}{\mu\rho})^{\frac{1}{4}}(m - m_\infty) \tag{39}$$

## 3.3 Region of action: Drying matter surface

### 3.3.1 Dielectric barrier effect

For a DC driven EHD setup, ions are produced near the metal electrode and move towards the drying material (which has dielectric properties) where they accumulate locally. The amount of accumulated charges on the surface increases, which can affect the dehydration through the surface of the material. This effect should be considered and requires further investigation. Some findings such as (Radu, Bartnikas and Wertheimer, 2003; Ohyama, Inoue and Chang, 2007) about this accumulated charge impact on EHD driven flow, approve the necessity of such a research.

In this regard, Radu and co-workers found that the trapped charge on the dielectric surface as well as the resulting field strongly reduces the velocity of the discharge propagation across the gap and increases the width of the discharge channel (Radu, Bartnikas and Wertheimer, 2003). Ohyama et al, reported that when the gas–liquid interface was exposed to gas-phase dc corona discharge, the corona wind was immediately stopped and the liquid-phase flow could not induce because the electric field strength at the needle electrode tip was decreased with increasing charge accumulation on the liquid free surface, i.e. dielectric barrier effect. Therefore, the liquid-phase EHD flow was not initiated by the gas-phase dc corona discharge under the applied voltage range (Ohyama, Inoue and Chang, 2007).

## 3.4 Region of action: Inside porous media (drying matter)

### 3.4.1 Electric double layer (EDL) and Electroosmotic flow (EOF):

Electric double layer (EDL) is a structure appears on the surface of an object when it is exposed to a fluid. The object might be a solid particle, a gas bubble, a liquid droplet, or a porous body (MacCurdy and Hod, 2016). Double layer refers to two parallel layers of charge surrounding the solid surfaces. Here in our case, this solid surface could be the pores or capillary surfaces inside the fruit tissue which contains water in liquid phase. EDL includes a compact layer of immobile

balanced charges and a diffuse layer of mobile ions. The first layer comprises ions strongly attracted to the substrate (i.e. hence immobile) due to chemical interactions. This layer is normally characterized by the Debye length, which typically has a value of 10 nm or less (Sheu, Kuo and Lin, 2012). The second layer is composed of ions attracted to the surface charge via the Coulomb force. This second layer is loosely associated with the object. It is made of free ions that move in the fluid under the influence of electric attraction and thermal motion rather than being firmly anchored. It is thus called the "diffuse layer" (MacCurdy and Hod, 2016). The interface between the compact (or Stern) layer and the diffuse layer, is called the shear plane.
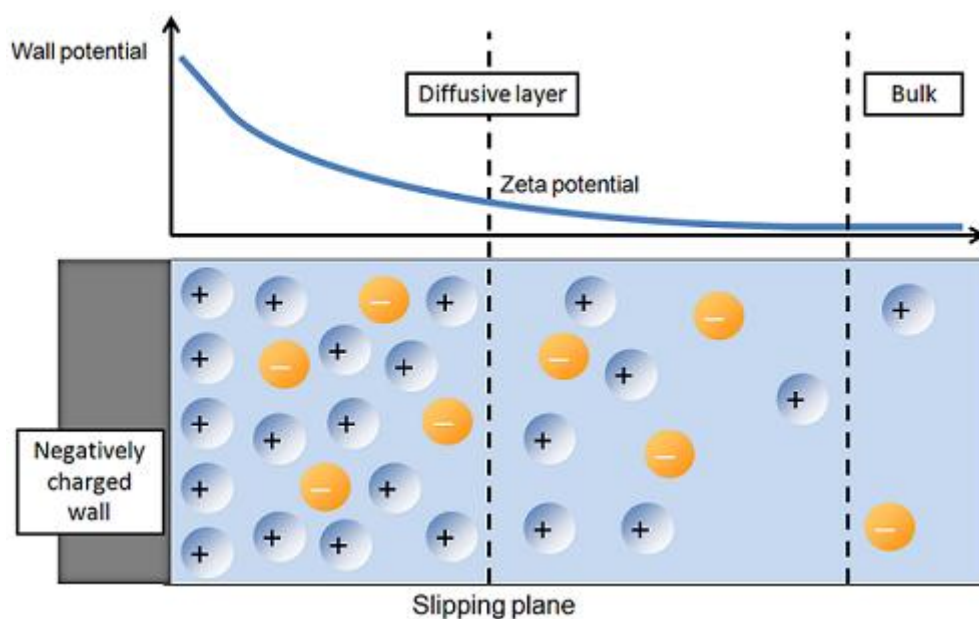


**Fig. 3-3 Schematic of EDL with specifying different layers**

In the diffuse layer, counter ions in excess can cause the fluid to convect under the externally applied force which is called Electroosmotic phenomenon that was observed by Reuss (Burgreen and Nakache, 1964). Electroosmotic flow (or Electroosmotic flow, often abbreviated EOF) is the motion of liquid induced by an applied potential across a porous material, capillary tube, membrane, microchannel, or any other fluid conduit. Electroosmotic flow is most apparent in systems with a large surface area to volume ratio, such as porous bodies with pores on the scale of micrometres to nanometres (Sheu, Kuo and Lin, 2012). When an electric field is applied across the liquid, the ions in the double-layer migrate in the field, which results in viscous drag to create bulk fluid flow and generation of a net pressure (MacCurdy and Hod, 2016). One of the most convenient utilization of the electroosmotic effect is in microfluidic pumps.

It has been recognized that high electrical fields employed for electroosmotic transport create both conduction and convection currents in the liquid. The convection current contributes to a net flow in the system, whereas the conduction current generates a volumetric Joule heating. Such Joule heating effects may not only cause local enhancements in temperature values, but also can create high temperature gradients (Chakraborty, 2006). The flow movement in the capillaries and Joule heating can affect the dehydration rate.

From another point of view, EDL is effectively a capacitor, which has a small electric potential called ζ across it. The zeta potential (typically 0.01 - 0.1 Volt), defined as the potential of the surface minus the potential just outside the double layer. (Hwang *et al.*, 2011).We can use this capacitor concept to model the EDL effect mathematically. Applying electric field E parallel to a flat surface, affects ions in the diffuse part of the double layer, which drag the fluid to produce an effective slip velocity outside the double layer. This velocity is given by the Helmholtz-Smoluchowski formula (Hunter, 2013),

$$u = -\mu_E E \tag{40}$$

Where

$$\mu_E = \frac{\varepsilon \zeta}{\eta} \tag{41}$$

ε being the permittivity and η viscosity of the fluid. For a capillary typical flow velocity of 100 μm/sec (1 mm/min) are produced by fields of 10 Volt/mm. It is noteworthy to mention that Electroosmotic flow mechanism is different from pressure-driven flows, since the flow speed is independent of channel radius. In contrast, pressure-driven (Poiseuille) flow down the channel produces a parabolic flow profile which decreases with miniaturization like the square of the radius due to viscous drag at the walls.

(Sheu, Kuo and Lin, 2012) developed a more in detail formulation by coupling equations for the hydrodynamic, electrical and thermal field variables. Joule heating is taken into account in the energy equation of his model. In addition to the inertia, viscous, and pressure gradient forces in the hydrodynamic system, the electrokinetic body force is also considered in the equations of motion for the calculation of solute acceleration and, then, the velocity in the resulting electrohydrodynamic system. For describing the ion and potential distributions in diffuse layer Poisson equation according to the theory of electrostatics is used:

$$\nabla^2(\varepsilon \Phi) = -\frac{\rho_e}{\varepsilon_0} \tag{42}$$

Where $\varepsilon_0$ ( $= 8.854 \times 10^{-12}$ C V$^{-1}$ m$^{-1}$) and $\varepsilon$ denote the permittivity of vacuum and fluid medium, respectively. $\Phi$ can be written as : $\Phi = \phi + \psi$ in which $\phi$ is externally applied electrical potential and $\psi$ is the electrical potential in EDL.

The derived equation by (Sheu, Kuo and Lin, 2012) is quite complex, but all the conservation equations for incompressible electrolyte solution, ionized fluid flow with the electroosmotic body force, the Laplace equation for the external electric field, the Poisson-Boltzmann equation for the zeta potential, and the conservation of energy with Joule heat can be cast into the following generalized form:

$$\bar{\phi}_t + u\bar{\phi}_x + v\bar{\phi}_y = \Gamma\nabla^2\bar{\varphi} + f \tag{43}$$

The definitions of all field variables $\bar{\phi}_i$, diffusivities $\Gamma$, and f are tabulated in **Error! R eference source not found.** provided by (Sheu, Kuo and Lin, 2012). Sheu et al (Sheu, Kuo and Lin, 2012) also applied these equation to a simple micro-channel (Fig. 3-5) to know how the applied electric field and the established electrical potential field in the solution due to attracting-and-repelling charges to/from the wall can affect the hydrodynamic behavior in the microchannel. The immobile positive ions are seen in the Stern layer and the mobile ions show their presence in the diffuse layer.

The working medium was considered as water-NaCl solution with the concentration of ($10^{-4}$ M), density of 1,000 kg m$^{-3}$, dielectric constant (78.4) and specific heat (4,180 J kg$^{-1}$ K$^{-1}$). It was concluded that the higher the electrical conductivity, the larger amount of Joule heat can be generated. More importantly, electroosmotic flow exhibits a much sharper streamwise velocity gradient near the wall than that predicted in the pressure-driven flow that is investigated at a fairly small Reynolds number. This shows the impact of electric field on fluid flow inside capillaries which can affect the dehydration as another driving force.

| | Continuity equation | Energy equation | x-momentum equation |
|---|---|---|---|
| $\bar{\phi}$ | $p$ | $T$ | $u$ |
| $\Gamma$ | $1$ | $\frac{k_1}{Pr\,Re}$ | $\frac{\mu}{Re}$ |
| $f$ | $-\left(\dfrac{\partial u}{\partial x}\right)^2-\left(\dfrac{\partial v}{\partial y}\right)^2-2\dfrac{\partial u}{\partial x}\dfrac{\partial v}{\partial y}+\dfrac{1}{Re}\left[\dfrac{\partial \mu}{\partial x}\left(\dfrac{\partial^2 u}{\partial x^2}+\dfrac{\partial^2 u}{\partial y^2}\right)+\dfrac{\partial \mu}{\partial y}\left(\dfrac{\partial^2 v}{\partial x^2}+\dfrac{\partial^2 v}{\partial y^2}\right)\right]$ $+\dfrac{\partial}{\partial x}\left(\dfrac{2Hzen_0\sinh(\psi)}{\rho U_{ref}^2}\dfrac{\partial \phi}{\partial x}\right)$ $+\dfrac{\partial}{\partial y}\left(\dfrac{2Hzen_0\sinh(\psi)}{\rho U_{ref}^2}\dfrac{\partial \phi}{\partial y}\right)$ | $\dfrac{H(\eta p_e+E_x\lambda(T))^2+H(\eta p_e+E_y\lambda(T))^2}{\rho c_p U_{ref}(T_0-T_{ref})\lambda(T)}$ | $+\dfrac{2Hzen_0\sinh(\psi)}{\rho U_{ref}^2}\dfrac{\partial \phi}{\partial x}+\dfrac{2n_0 k_b T\sinh(\psi)}{\rho U_{ref}^2}\dfrac{\partial \psi}{\partial x}$ |

| | y-momentum equation | Electric equation | Zeta potential |
|---|---|---|---|
| $\bar{\phi}$ | $v$ | $\phi$ | $\psi$ |
| $\Gamma$ | $\frac{\mu}{Re}$ | $\lambda$ | $\varepsilon$ |
| $f$ | $-\dfrac{2Hzen_0\sinh(\psi)}{\rho U_{ref}^2}E_y+\dfrac{2n_0 k_b T\sinh(\psi)}{\rho U_{ref}^2}\psi_y$ | $0$ | $\dfrac{2H^2 z^2 e^2 n_0}{k_b T\varepsilon_{ref}\varepsilon_0}\sinh(\psi)$ |

**Fig. 3-4 Summary of the transport equations shown in equation (34) (adopted from (Sheu, Kuo & Lin 2012b))**
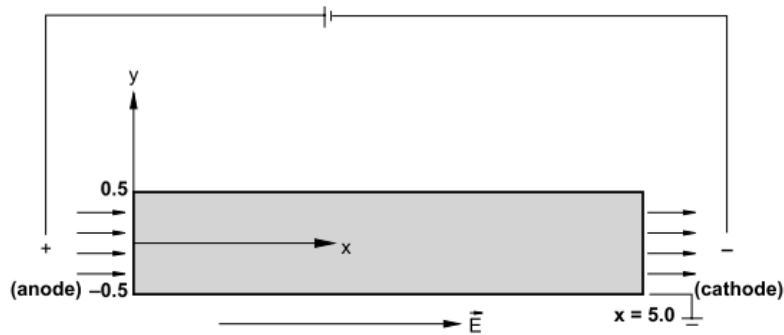
**Fig. 3-5 Schematic of the microchannel investigated by(Sheu, Kuo & Lin 2012b)**

### 3.4.2 Electro/Dielectrophoresis effect

The mobility of the particles in suspension can be a result of forces acting directly on them or of the drag from the moving liquid around them. The electric field driven mobility of the particles and of the liquid can be classified in four broad categories. (Velev and Bhatt, 2006) describes these four groups of electric field driven as presented in Fig. 3-6. (a) Electrophoresis; is the motion of dispersed particles relative to a fluid under the influence of a spatially uniform electric field usually in DC. (b) electroosmosis; liquid flows are driven by the moving counter-ionic layer near the wall between the electrodes (already discussed in previous sections). (c) Dielectrophoresis (DEP); is the movement of a particle in a non-uniform electric field due to the interaction of the particle's dipole and spatial gradient of the electric field usually occurs in AC field but can happen even in non-uniform DC. (d) AC Electrohydrodynamics—liquid flows are generated at the walls near the electrodes by the gradient of the field.
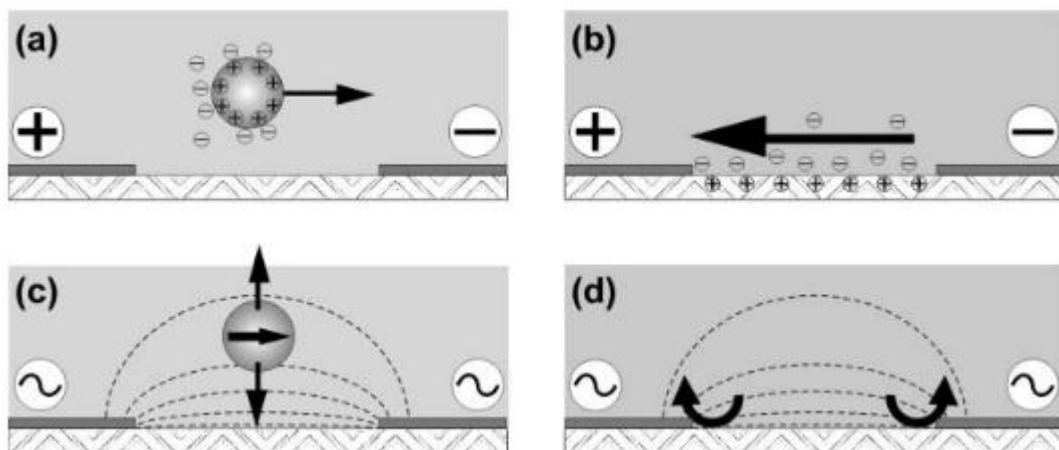


**Fig. 3-6 Schematics of the four groups of electric field driven effects taking place under the action of DC and AC fields adopted from (Velev & Bhatt 2006)).**

Electric field in an ionic media (such as water) creates a complex effect in fluid movement. The fluid flow velocity will be equal to the one caused by the electrophoretic or Dielectrophoretic effect, plus the electroosmotic velocity (which changes with the position inside the cell) (Velev and Bhatt, 2006).

As it was discussed in the Chapter 2:, 2nd term of the electric force (equation (11)) stands for Dielectrophoretic force. It is composed of a force density that arises from the non-uniformity of the material properties and a force density that can be combined with the hydrodynamic pressure. The DEP force arises via interaction of the induced dipoles with the gradient of the (inhomogeneous) field. The resultant force, $F_{DEP}$, is dependent on the gradient of the field squared, $\nabla E^2$ and the particle radius cubed (i.e., proportional to particle volume) (Velev and Bhatt, 2006). The electrophoretic mobility formulation for different particle size and zeta potential is given in (Velev and Bhatt, 2006). Moreover, (Çetin and Li, 2011) introduces two methods to calculate the DEP force on a particle, (i) point-dipole method and (ii) Maxwell-stress tensor (MST) formulation. Based on (Velev and Bhatt, 2006):

$$F_{DEP} = 2\pi\varepsilon_1 r^3 \nabla E^2 Re|K| \tag{44}$$

Where K is Clausius–Mossotti function. The sign and magnitude of this $F_{DEP}$ are dependent on the effective polarizability of the particle, which is described by the real part of K.

$$Re|K| = \frac{\varepsilon_2 - \varepsilon_1}{\varepsilon_2 + 2\varepsilon_1} + \frac{3(\varepsilon_1 \sigma_2 - \varepsilon_2 \sigma_1)}{\tau_{MW}(\sigma_2 + 2\sigma_1)^2(1 + \omega^2 \tau_{MW}^2)} \tag{45}$$

In the above formulae, $\varepsilon_1$ and $\sigma_1$ are the dielectric permittivity and conductivity of the media and $\varepsilon_2$ and $\sigma_2$ that of the particles.

Suppose that L denotes the length that characterizes the electrical field variations and $\phi$ denotes the applied voltage to the system. For a fixed size of particle, an order of magnitude estimate of DEP force using (44) would lead to

$$F_{DEP} \sim \frac{\phi^2}{L^3} \tag{46}$$

By using the same approach, temperature rise of the system as a result of the Joule heating can be written as (Çetin and Li, 2011):

$$\Delta T \sim L^2 E^2 \tag{47}$$

## 3.4.3 Surface tension effect

It has been proved that surface tension of liquids can be affected in presence of electric field. In this section, three underlying phenomena that have impact on surface tension variation due to electric field.

### 3.4.3.1 Thermocapillary (Marangoni) forces

When a free liquid surface is present, the surface tension variation is resulting from the temperature gradients along the surface. Surface tension can also change with concentration variation. The unbalance surface energy can induce a motion within the fluid which is called thermocapillary flow (thermal Marangoni convection) (Moatimid and Hassan, 2013). Thermocapillary or so-called Marangoni forces are one of the principal forces affecting the fluid flow (Lee, Quested and McLean, 1998). The system tends to minimize its surface energy in expanding regions of lower interfacial tension towards regions of higher interfacial tension (i.e. surface flow occurs from regions of low to high surface tension). The incipient motion of the interface provokes an additional tangential shear stress component on curved surfaces such as droplets or bubbles. As a consequence, a motion of the fluid layers adjacent to the interface is induced (Wegener and Paschedag, 2011)),

Some established well-known mass transfer models due to Marangoni effect are shown in Fig. 3-7. In this figure $C^*$ is the related concentration of the transferred solute A in the droplet: $C^* = \frac{\bar{C}_A - mC_{AC\infty}}{C_{Ad0} - mC_{AC\infty}}$ with the mean solute concentration in the droplet $\bar{C}_A$, the distribution coefficient m, the solute concentration in the continuous phase, far away from the droplet $C_{AC\infty}$, and the initial solute concentration in the droplet $C_{Ad0}$.

| Author(s) | Related concentration | Eq. |
|---|---|---|
| Newman (1931) | $c^* = \frac{6}{\pi^2} \sum_{n=1}^{\infty} \frac{1}{n^2} \exp\left[-4\frac{(n\pi)^2 D_A t}{d_P^2}\right]$ | (3) |
| Kronig and Brink (1950) | $c^* = \frac{3}{8} \sum_{n=1}^{\infty} B_n^2 \exp\left[-64\frac{\lambda_n D_A t}{d_P^2}\right]$ | (4) |
| Calderbank and Korchinski (1956) | $c^* = 1 - \left(1 - \exp\left[-R\frac{4\pi^2 D_A t}{d_P^2}\right]\right)^{1/2}$ | (5) |
| Handlos and Baron (1957) | $c^* = \exp\left[\frac{-\lambda_n v_t t}{128 d_P (1+\mu^*)}\right]$ | (6) |
| Henschke and Pfennig (1999) | $c^* = \frac{6}{\pi^2} \sum_{n=1}^{\infty} \frac{1}{n^2} \exp[-(n\pi)^2 Fo']$ | (7) |

**Fig. 3-7 Mathematical models to predict mass transfer in the dispersed phase (spherical droplets, no resistance in the continuous phase).**

42

(Wegener and Paschedag, 2011) mentions that using the Henschke and Pfennig (with $C_{IP}$ = 3400) and the Calderbank and Korchinski (with R = 13) models, mass transfer is enhanced by a factor of about five compared to non-Marangoni dominated systems. (Moatimid and Hassan, 2013) studied the EHD Marangoni convection in the presence of an axial electric field through a micro cylindrical porous flow. Their model showed stabilizing effect of electric field on the interface according to the changing the surface tension. Changing the liquid fluidity can impact the dehydration rate. Therefore Marangoni effect can be considered as another EHD drying driving force.

### 3.4.3.2 Electrocapillarity

Electrocapillary phenomenon refers to the modification of the interfacial tension by the presence of electrical charges. The first comprehensive investigations on electrocapillary phenomena were performed by Lippman, in 1875 (Chakraborty, 2014). In comparison to its thermal counterpart (i.e., the thermocapillary effect), electrocapillary respond faster to the applied electric field with possible characteristic timescales of even less than a few milliseconds. At the micron length-scale, the interfacial tension forces dominate a droplet's hydrodynamic behavior. They include a force on the two-fluid interface between the droplet and the ambient fluid, and a force on the tri-phase contact line where the droplet, the ambient fluid, and the solid meet.. Electrocapillary force creates a non-uniform interfacial tension at the two-fluid interface. The induced interfacial shear flow can be used to move the droplets. Note that, there is a difference between the electrophoretic force and Electrocapillary force. The electrophoretic force arises from a non-zero $\rho_e$ in the bulk; and the Electrocapillary force arises from a non-zero $\rho_e$ at the interfaces (Zeng and Korsmeyer, 2004).

There are three types of electrocapillary principles namely, continuous electrowetting (CEW), electrowetting (EW), electrowetting on dielectrics (EWOD) (Zeng and Korsmeyer, 2004; Chakraborty, 2014). In CEW a motion of the droplet can be actuated, because of the establishment of a pressure differential on account of an asymmetric change in the interfacial tension and a consequent asymmetric deformation of the two menisci. Electrowetting (EW) acts only on tri-phase contact line. When a droplet is in contact with a solid electrode, a wetting force may arise upon application of an electric field. This wetting force acts on the tri-phase contact line and causes the contact angle reduction that is usually observed in experiments. In EWOD in the liquid and the electrodes are separated by a thin dielectric layer.

A fundamental postulate that is common to the three basic electrocapillary actuation principles, mentioned as above, is the change in surface energy with the application of electrical potentials, as governed by the Lippmann -Young theory which is commonly used in Electrocapillary research (Chakraborty, 2014).

$$\gamma = \gamma_0 - \frac{1}{2}cV^2 \tag{48}$$

$$E = \sum_{i \neq j} A_{ij}\gamma_{ij} - \lambda \forall \tag{49}$$

where $\gamma_0$ is the surface tension when there is no voltage applied across the interface and c is the capacitance per unit area of the EDL (for CEW and EW) or the dielectric layer (for EWOD). $\forall$ is the droplet volume and $\lambda$ is a Lagrange multiplier to enforce a constant volume constraint (physically, $\lambda$ is equal to the pressure drop across the liquid–vapor interface, thermodynamically consistent with the definition of free energy of a system). Here $A_{ij}$ is the interfacial area that demarcates the phases i and j, with the corresponding surface energy being designated as $\gamma_{ij}$.

Chakraborty (Chakraborty, 2014) did an in detail analytical calculation and he defined equivalent electrocapillary pressure ($p_{ec}$) as:

$$P_{ec} = \frac{l\Delta\gamma}{A_c} = \frac{l}{A_c}\frac{1}{2}\varepsilon_d\frac{V^2}{d} \tag{50}$$

Where $l$ is inner circumference of the conduit handling the liquid droplet and $A_c$ is the cross-sectional area. Using Navier-Stokes equation the following velocity profile can be obtained:

$$u = \frac{1}{\mu H}\frac{d\gamma}{dx}(y^2 - Hy) \tag{51}$$

And for the case of a cylindrical capillary, he used the Newton's second law of motion of the advancing droplet (neglecting the inertial effects and assuming a fully developed velocity profile) and from experimental correlation, the net driving force for initiation of the droplet motion can be modeled as:

$$F = 2\pi R\gamma_{lv}BCa^x \tag{52}$$

Where Ca is the capillary number ($Ca = \mu\bar{u}/\gamma_{lv}$) and B and x are experimentally fitted constants. By affecting the velocity field and exerting a new force to the liquid inside porous media, the dehydration can be facilitated.

### 3.4.3.3 Electroporation

Electroporation, or electropermeabilization, is a microbiology technique in which an electrical field is applied to cells in order to increase the permeability of the cell membrane of the bilogical tissue. Recently, pulsed electric fields (PEF) have demonstrated effectiveness in non-thermal electropermeabilisation (electroporation) of microorganisms and membranes of food plants. This excitation of the cell membrane should be taken into account for further research about its impact on cell dehydration.

## Chapter 4: EHD drying device simulation

There is a promising potential of EHD drying for industrial scale application (Bajgai *et al.*, 2006; Martynenko and Kudra, 2016b; Defraeye and Martynenko, 2019), where even an EHD-enhanced drying prototype was introduced(Lai, 2010). However, still little is known on the driving mechanisms of EHD-drying (Martynenko *et al.*, 2017) as well as up-scalable dryer configurations, which have hindered commercial exploitation of this technology. The exact contribution of different mechanisms of energy and mass transfer in EHD drying are currently not well known (Martynenko and Kudra, 2016b). However, the main enhancement of convective mass transfer is attributed to the EHD-generated airflow (ionic wind)(Martynenko *et al.*, 2017; Defraeye and Martynenko, 2018). Several investigations have been carried out to adjust the electrode configuration and geometrical parameters, as well as operating parameters (e.g. voltage), to enhance the EHD airflow rates. Almost all researches, however, targeted a wire/needle-to-plate configuration (Fylladitakis, Theodoridis and Moronis, 2014; Misra *et al.*, 2018). This configuration has been demonstrated to not be the optimal configuration for drying of large amounts of products simultaneously or uniformly (Defraeye and Martynenko, 2019). Recently, Defraeye and Martynenko (Defraeye and Martynenko, 2018) revealed the significant advantages in drying rates of a wire-to-mesh compared with the wire-to-plate emitter-collector configuration (Fig. 4-1). The reason is that this configuration enables the airflow to pass over the drying material, hence taking all moisture with it, by which it does not affect any other products. It also leads to a relatively uniform drying on all surfaces and hence less drying time. This first step in evaluating the mesh collector however modeled it in a very idealized way, namely as a homogeneous, highly-porous, grounded zone without discretely accounting for the mesh wires. Due to their large curvature, these individual wires could have an impact on the Coulomb force generation and distribution around the product to be dried.

To further utilize the mesh collector concept in an industrial scale, a more realistic representation of the mesh is required. This can help explore possible optimizations of the size, number and location of the wires of the collector electrode, as the electric field intensity, Coulomb force and resulting airflow around the drying material are more realistic. An improved collector design could be sought in that way with the best tradeoff between shortening the drying time and reducing the energy consumption.
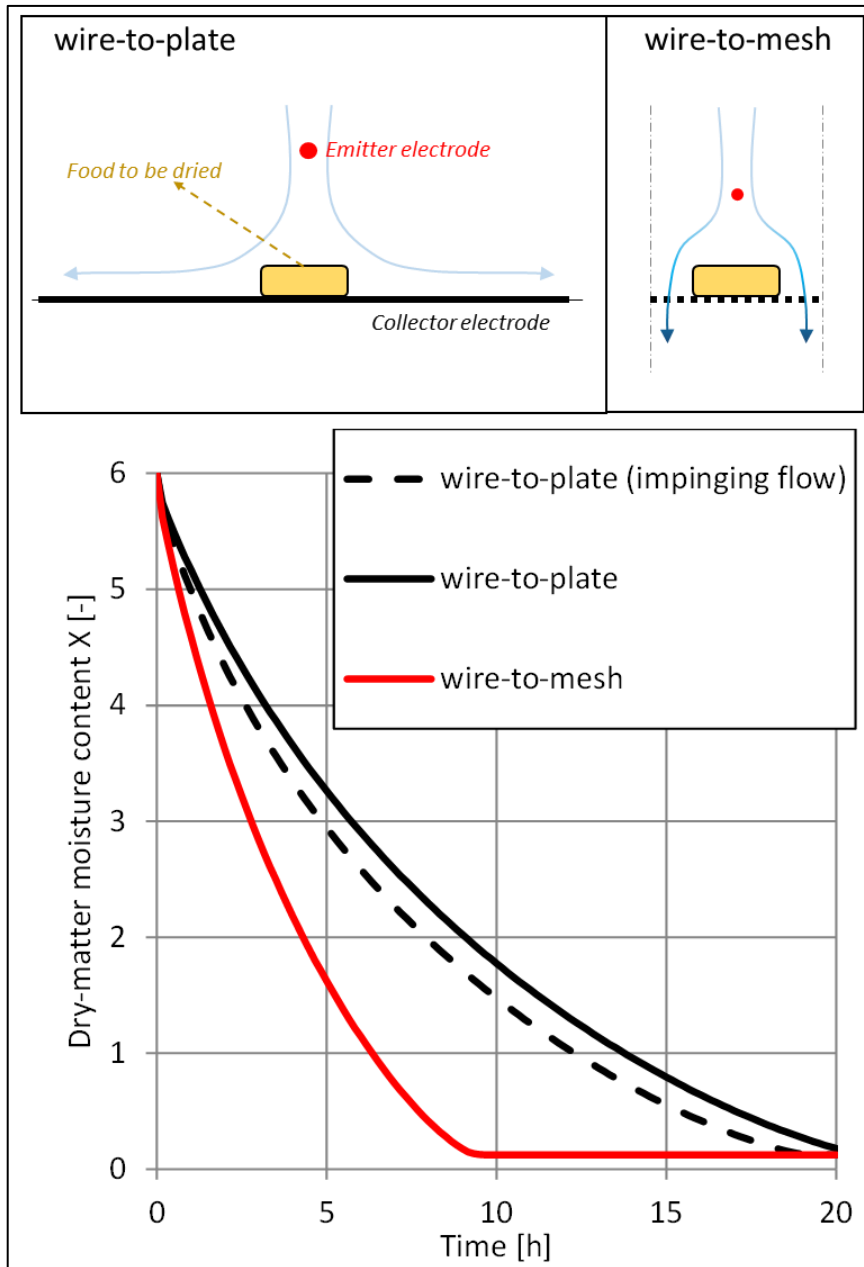
**Fig. 4-1 Comparison of Wire to mesh and Wire to plate configurations (**(Defraeye and Martynenko, 2019)**)**

Accordingly, in this chapter, the impact of various mesh parameters (wire diameter, wire number and porosity) on the electric field intensity, the resulting Coulomb force on the air flow and the drying rate was explored. Moreover, the in detail distribution of important parameters such as Coulomb force and electric field, around the drying matter, has been quantified and discussed. In addition, it is shown that the critical drying time which is introduced by (Defraeye and Verboven, 2017), is not enough for comparing different EHD drying devices, therefore a new thorough performance index has been introduced.

## 4.1 Configurations related to mesh parameters study

As a further step towards a realistic model of wire to mesh configuration, mechanistic modeling of mesh should be used. This can help to evaluate the size, number and location of the wires of the collector electrode, for explore possible optimizations as the electric field intensity, Coulomb force and resulting airflow around the drying material become more realistic. Another important mesh parameter is porosity of the mesh. The porosity, $\beta$, can be defined as the screen's open area ratio:

$$\beta = (1 - \frac{d_w}{l})^2 \tag{53}$$

where $d_w$ is the wire diameter and $l$ is called the mesh length which is the center to center distance between 2 wires. If we consider $d_w$ as variable, in order to keep the porosity constant, the number of the wires has to change according to the variation of $d_w$. The porosity should be a reasonable value in such a way that the wires are separated by a distance wide enough for low airflow blockage and small enough for holding the samples properly. To this end, 3 mesh porosities of approximately 85, 70 and 50 percent, are considered for this study (Fig. 4-2). The wires diameter and number for different case studies vary according Table. 4-1. The different mesh porosities are compared to the ideal mesh with a porosity of 100%. Short names for different case studies have been considered in which the first number represents the porosity, second and third numbers are related to the number and diameter of the wires, respectively (Table. 4-1).
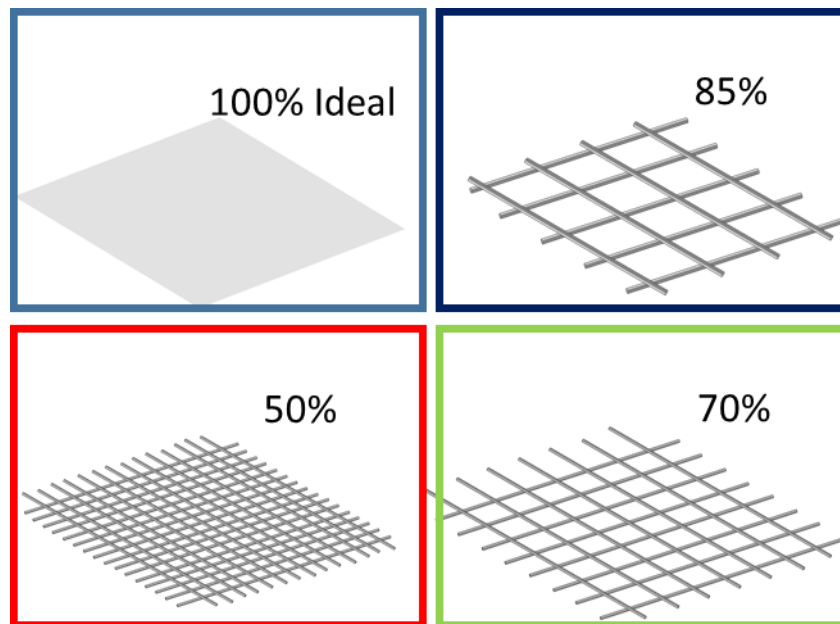


**Fig. 4-2 Schematic of different mesh porosities considered for this study**

If we divide whole the EHD drying process into two principal sub-processes of 1-EHD flow generation and 2- dehydration, by taking into account all the mathematical modeling considerations mentioned in the previous chapters, it is clear from the equations (1 to 11), that electric field E, and flow field u, have the most important role in EHD flow generation (1$^{st}$ sub-process). About the second sub-process, as a matter of fact, flow distribution around the sample has the highest impact on the convection mechanism. Hence, in whole the EHD drying process, effective distribution of electric field and airflow are the key points to have more uniform dehydration and less drying time in this model.

**Table. 4-1 Studied mesh configurations in terms of porosity and geometrical parameters**

| Case study name | Wire Number | $d_w$ [µm] | Porosity [%] |
|---|---|---|---|
| Ideal Mesh | ∞ | 0 | 100 |
| P85_N23_D1000 | 23 | 1000 | 85.2 |
| P85_N46_D500 | 46 | 500 | 85.2 |
| P85_N75_D300 | 75 | 300 | 85.5 |
| P85_N97_D240 | 97 | 240 | 85.1 |
| P70_N46_D1050 | 46 | 1050 | 70.4 |
| P70_N97_D500 | 97 | 500 | 70.3 |
| P50_N46_D1900 | 46 | 1900 | 50.2 |
| P50_N97_D900 | 97 | 900 | 50.3 |

Of course if the other dehydration mechanisms were included in this model, other factors could be important too. Nevertheless, the authors believe that in the presence of all the driving forces of dehydration, electric field intensity and ionic flow distribution still play the most important role. Since most likely, all the known and unknown driving forces for mass and heat transfer in EHD drying are somehow related to electric field intensity, airflow field, and charge distribution. Although according to Eq. (2), (4), (10) and (11), these three parameters have mutual effects on each other, but it is clear that electric field intensity has the highest impact as it drives the flow field (Eq. (10) and (11)), and both of these two equations, influence the charge distribution. Therefore, effective electric field intensification and flow distribution around the product are important not only for convective dehydration models (the current study) but also in the future studies with more complete model including the other dehydration mechanisms.

As mentioned before, this intensified electric field could excite more and increase the effect of other dehydration mechanisms if they were included in the model.
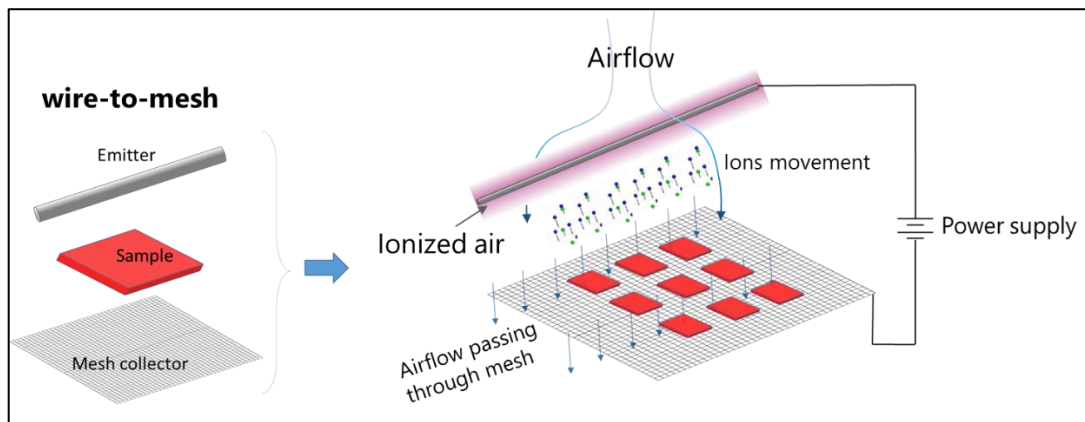


**Fig. 4-3 Schematic of EHD dryer with Wire to mesh configuration considered for the simulation**

## 4.2 Results and discussion

Dehydration behavior of the drying material is a function of CMTC on the material boundaries. Obviously, CMTC variation depends on CHTC and airflow distribution around the material. In EHD driven flows, the flow field behavior relies on electrostatic forces, that based on Eq. (12) are the result of SCD and electric field interaction. Therefore, in this part, we follow the same procedure to discuss the results in a clear way, by starting from the flow field analysis and going to the electric field and SCD evaluation in order to explain the different drying rates and CHTCs for different configurations.

In order to have a general vision of the simulation, some results for one of the case studies (P85_N23_D1000) are presented in Fig. 4-4 to Fig. 4-6. In Fig. 4-6 the transient airflow evoulution after activation of the device is shown. The flow becomes steady after almost 60s. The results of the steady flow have been use to feed the dehydration equations boundary conditions and inputs.

**Fig. 4-4 a) Temperature distribution around the drying matter (steady state) b) isothermal contour lines**



**Fig. 4-5 a) Electric field lines between emitter and collectors b) Steady state pressure contours**

**Fig. 4-6 Airflow evolution after activation of the device**

52

### 4.2.1 Mesh parameters impact

The main goal of this section is to evaluate the influence of mesh collector parameters on the electrostatic conditions and 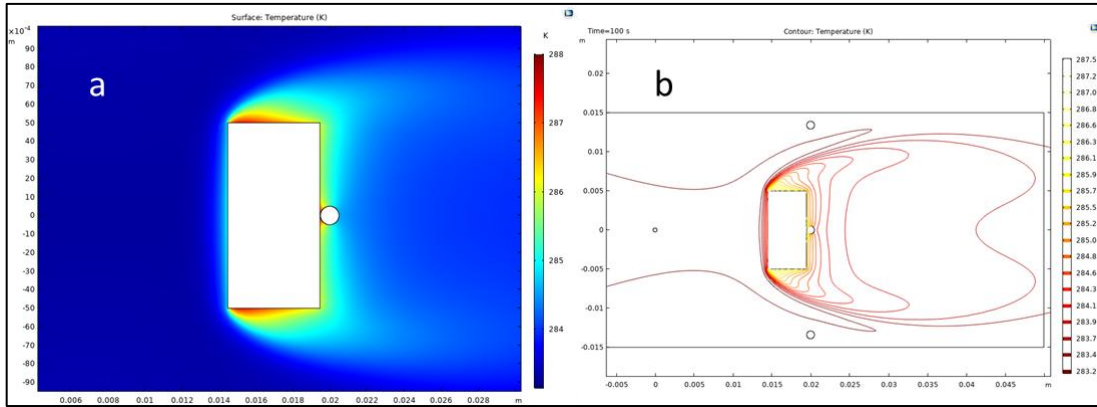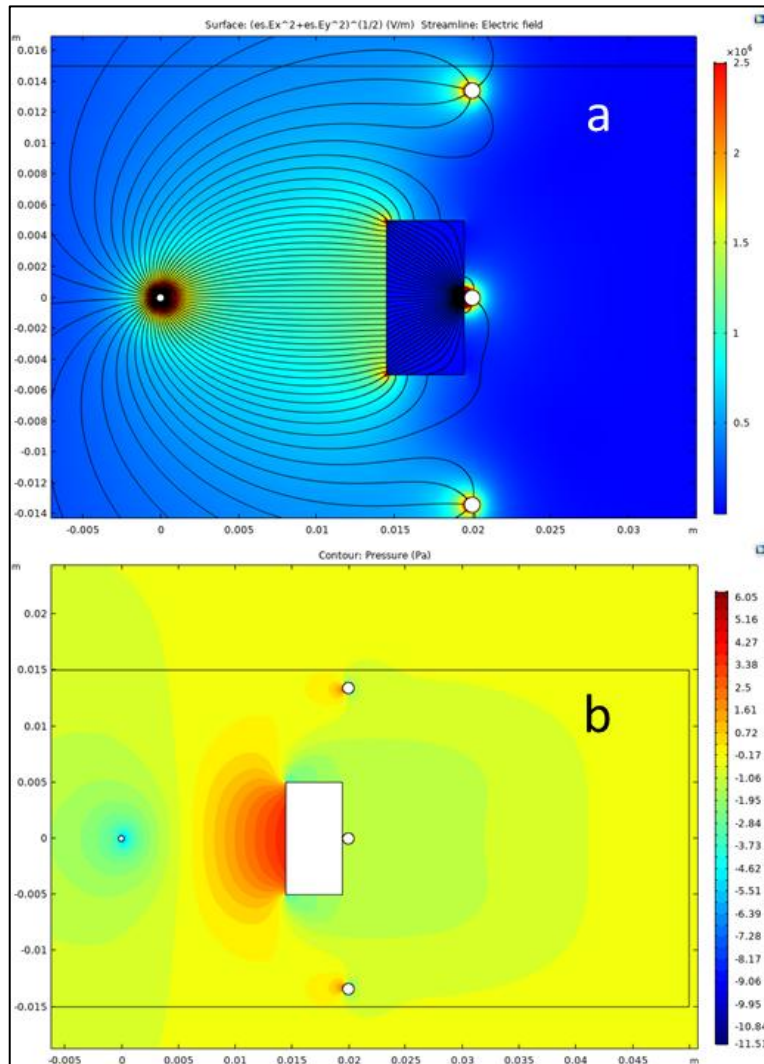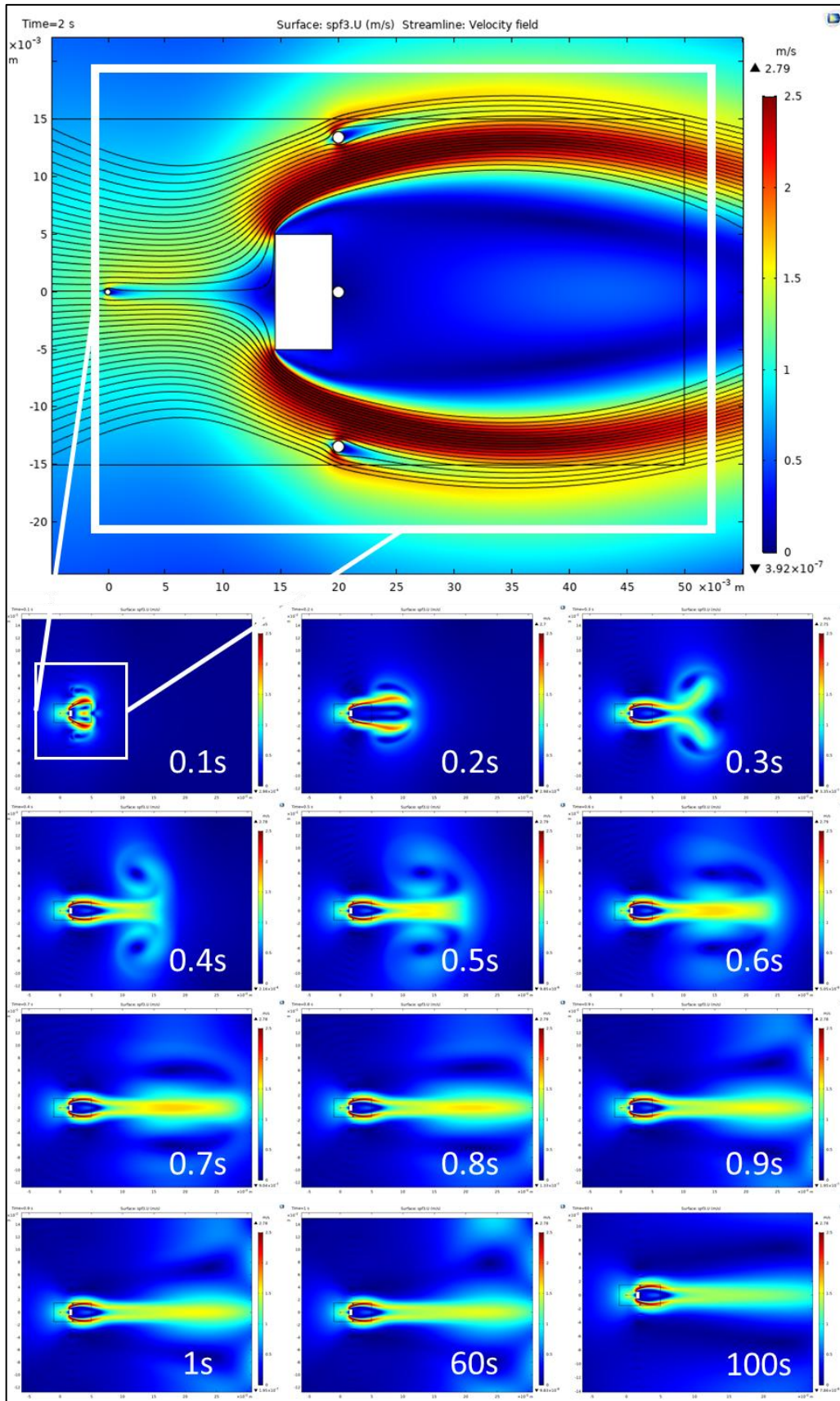the consequent drying behavior of the food. The wires are discretely modeled with realistic values of diameter and number. First, mesh porosity variation is considered. It is well clear that different mesh porosities affect the airflow distribution (Laws and Livesey, 1978; Brundrett, 1993). The aim here is to see how this variation of airflow distribution affect the drying kinetics when the mesh is a collector as well. Second, different combinations of wire diameter and number for the same porosity have been explored. The aim is to investigate the effect of wire diameter and number for a constant mesh porosity as the curvature of the collector wires affects the electrostatic conditions.

### 4.2.2 Mesh porosity effect

Three different mesh porosities of 50%, 70% and 85% have been modeled to see their effects on drying kinetics of the fruit. The drying curves for the different mesh porosities as well as their CHTC values on the sample boundaries are depicted in Fig. 4-7 and Fig. 4-8. In order to have a quantitative evaluation, the most important parameters such as $t_{crit}$, airspeed, and average value of electrostatic parameters are calculated (Table. 4-2). Moreover, the electrostatic parameters distribution as well as the resulting airspeed distribution in the region of interest, are shown in Fig. 4-10.

All the configurations for different mesh porosities show almost the same drying behavior with slightly and negligible difference in critical drying time (Fig. 4-7a). However, compared to the ideal mesh, there is more than 2 hours difference in critical drying time ($\approx$ 30% difference). The CHTC plots (Fig. 4-7b) show 3 different level of lines. The differences in CHTCs arise from airflow distribution around the drying matter (Fig. 4-10d). The maximum airspeed for all the discrete-modeled meshes (porosity lower than 100%) is higher compared to the ideal mesh. Nonetheless, the airspeed gradient in y-direction (Fig. 4-10d) is lower for the Ideal case (compared to the other configurations), which results in higher average airspeed around the fruit (Table. 4-2).

The maximum values of airspeed result in higher CHTC on the corners of the fruit (peaks in Fig. 4-7b), but the average CHTC is correlated with the average airspeed (Table. 4-2). This gives a hint for designing the optimal mesh configuration, for which having a high average airspeed should be considered. Accordingly, higher average airspeed with low gradient is considered as effective airflow distribution. This result, from one hand, proves the importance of effective

flow distribution around the sample, and from the other hand, shows the impact of pressure drop due to mesh porosity, as it will be discussed later.
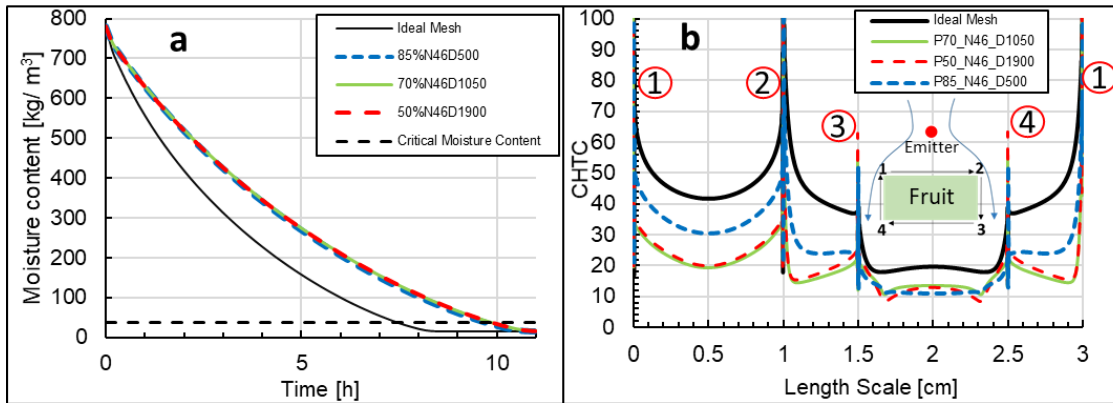


**Fig. 4-7 Different mesh porosity vs. ideal mesh: a) sample moisture content b) CHTC as a function of sample boundary length (only for some of the simulated case studies)**
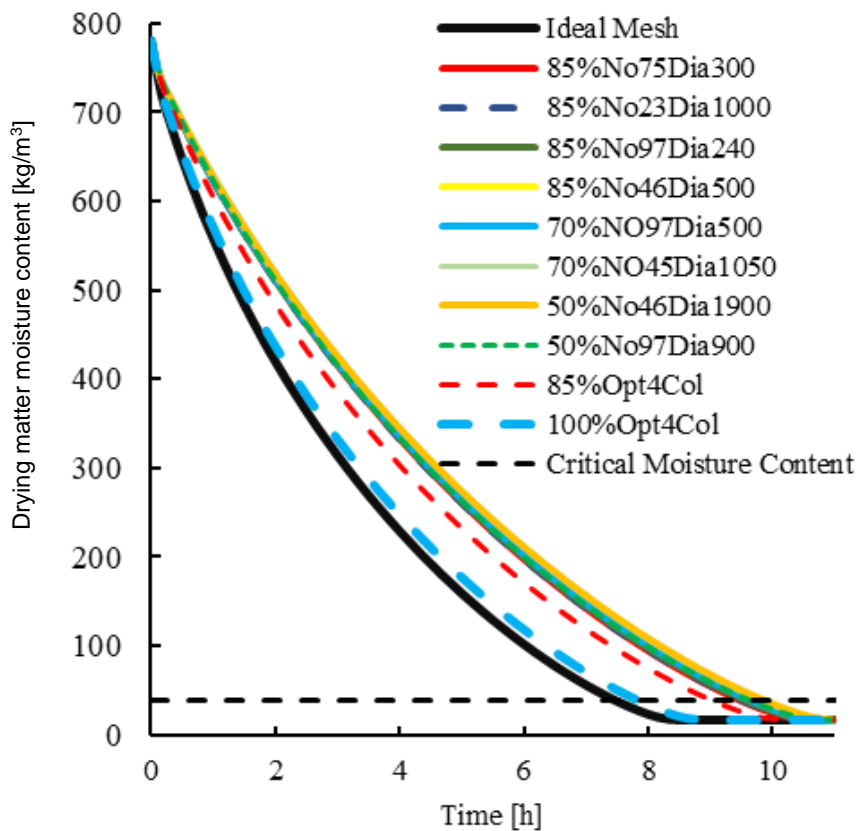


**Fig. 4-8 sample moisture content for all the simulated cases**
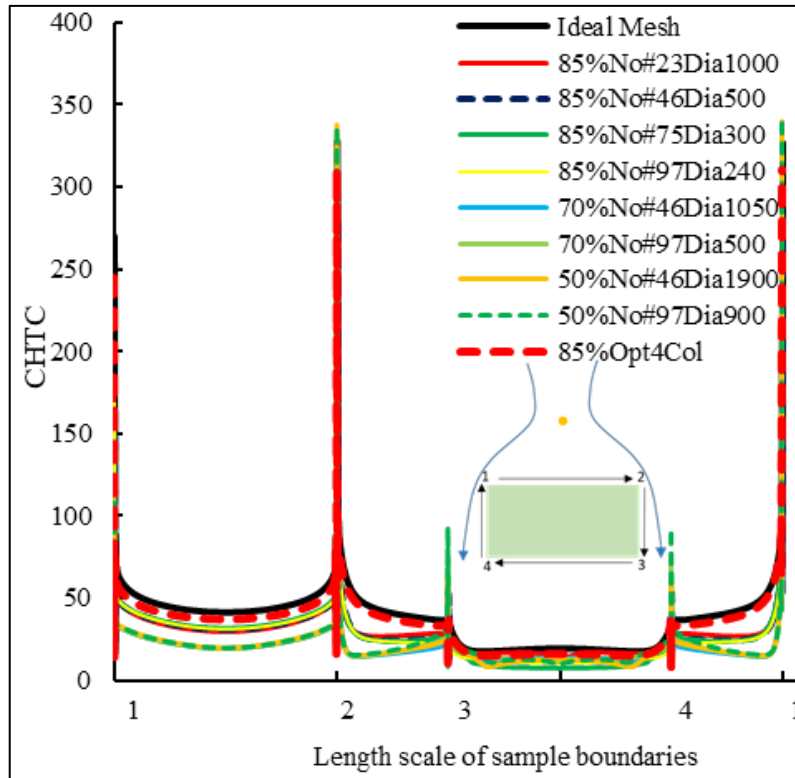
**Fig. 4-9 CHTC as a function of sample boundary length for all the simulated cases of**

According to Table. 4-2, for all the electrostatic parameters, namely Coulomb force, electric field intensity, and space charge density, the Ideal mesh provides lower average values in the region of interest compared to other configurations; nevertheless, the average airspeed is higher. Coulomb force distributions in all the configurations are almost similar except near the wire collectors that its intensity increases due to the higher collector curvature at those regions. Similar electrostatic conditions but different flow field and drying characteristics between Ideal case and others brings us to this conclusion that the pressure drop due to the volume of the wires, is the missing link in this analysis.

The first term in the right-hand side of Eq.(10) represents the effect of the pressure gradient in Navier-Stokes equation. As the porosity of the mesh decreases, the pressure decreases after the mesh. This pressure drop, reduces the local velocity behind the mesh and due to the upstream propagation of disturbances in subsonic airflows. All of these changes result in lower CHTC hence, higher drying time. However, the uniform drying of the fruit, which is one of the main advantages of mesh collector configuration over other configurations, remains the same. The authors believe that in the real case this difference in the critical times between the ideal mesh and non-ideal meshes could be lower as

the intensified electric field close to the sample would excite other drying mechanisms as well.
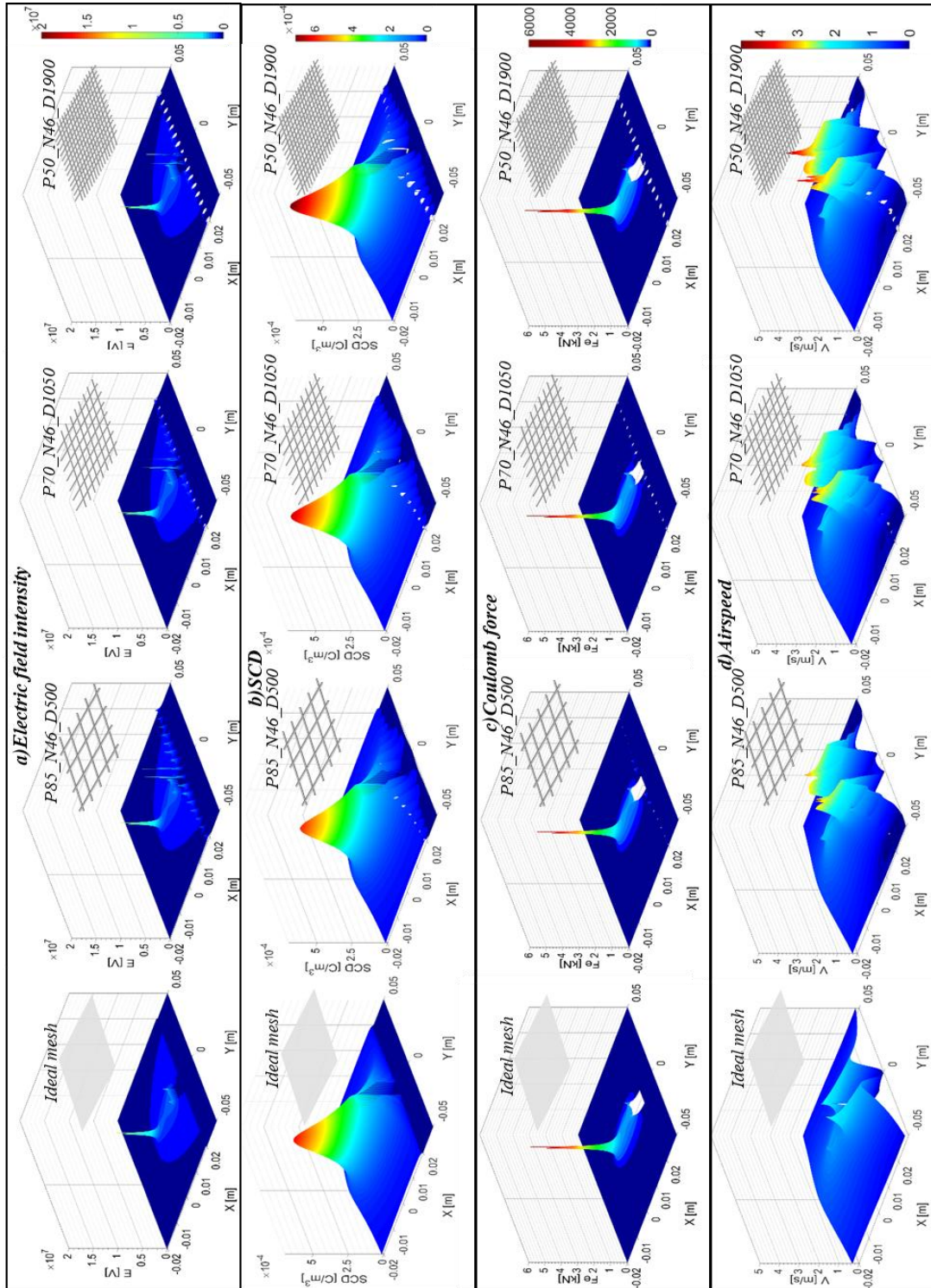


Fig. 4-10 Distribution of electrostatic parameters and resulting airspeed in the region of interest

**Table. 4-2 Quantitative evaluation of the most important parameters for different mesh porosities**

| | Porosity [%] | $t_{crit}$ [h] | Average CHTC [W/m²K] | Maximum air speed [m/s] | Average airspeed* [m/s] | Average $F_e$* [N] | Average E*[V] | Average SCD* [C/m³] |
|---|---|---|---|---|---|---|---|---|
| Ideal Mesh | 100 | 7.47 | 37.49 | 2.32 | 0.67 | 20.29 | $2.55 \times 10^5$ | $7.96 \times 10^{-5}$ |
| P85_N46_D500 | 85 | 9.72 | 19.20 | 3.18 | 0.57 | 21.15 | $2.57 \times 10^5$ | $8.22 \times 10^{-5}$ |
| P70_N46_D1050 | 70 | 9.70 | 19.13 | 3.29 | 0.58 | 22.19 | $2.61 \times 10^5$ | $8.51 \times 10^{-5}$ |
| P50_N46_D1900 | 50 | 9.89 | 19.46 | 4.18 | 0.58 | 22.68 | $2.60 \times 10^5$ | $8.72 \times 10^{-5}$ |

*in the region of interest

Normally, decreasing the porosity increases the pressure loss in an ordinary mesh(Brundrett, 1993; Annand, 2016), but this is not the case in mesh collector configuration since by decreasing the porosity the collector surface increases that results in higher average electric field intensity, SCD and finally higher Coulomb force (Table. 4-2). Therefore, changing the porosity doesn't have a very significant effect on critical drying time while the electrostatic conditions change. However, if we compare the specific energy consumptions (Fig. 4-11), the difference will be revealed. By decreasing the porosity energy consumption per unit mass of drying matter increases.
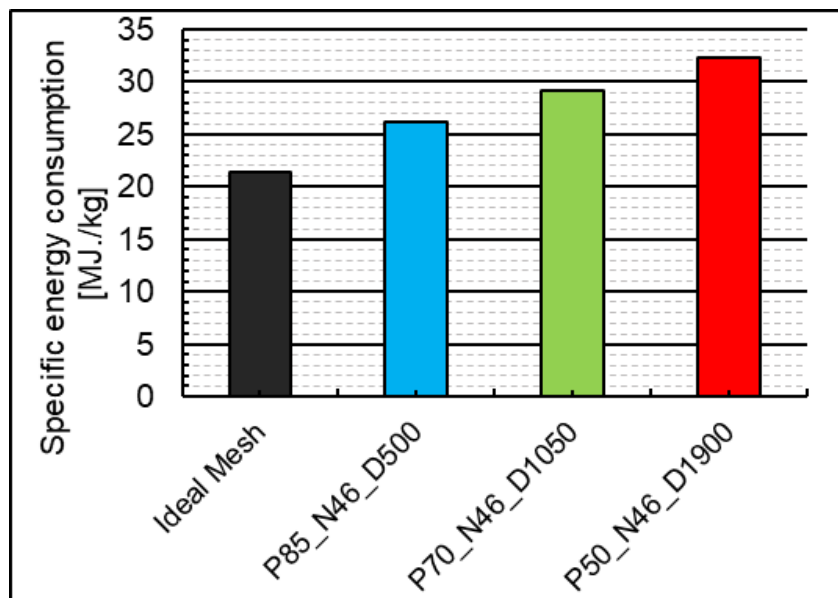


**Fig. 4-11 Specific energy consumption for different mesh porosities**

### 4.2.3 Wire number and diameter effect

Keeping the same porosity, the effect of wire diameter and numbers on drying kinetics was investigated. The most important parameters in different physics are shown in Table. 4-3. Even though the impact of wire diameter on the drying time is not very striking, however, the lower the wire diameter, the higher the average CHTC and the lower the drying time.

**Table. 4-3 Quantitative evaluation of the most important parameters for different wire numbers and diameters**

| | Porosity [%] | $t_{crit}$ [h] | Average CHTC [W/m$^2$K] | Maximum Airspeed [m/s] | Average Airspeed* [m/s] | Average $F_e$* [N] | Average E*[V] | Average SCD* [C/m$^3$] |
|---|---|---|---|---|---|---|---|---|
| P85_N23_D1000 | 85 | 9.56 | 19.83 | 2.78 | 0.56 | 20.73 | 2.56 E+05 | 8.10 E-05 |
| P85_N46_D500 | 85 | 9.72 | 19.20 | 3.18 | 0.57 | 21.15 | 2.57 E+05 | 8.22 E-05 |
| P85_N75_D300 | 85 | 9.58 | 19.75 | 2.91 | 0.58 | 21.23 | 2.57 E+05 | 8.25 E-05 |
| P85_N97_D240 | 85 | 9.46 | 21.95 | 3.18 | 0.59 | 21.16 | 2.58 E+05 | 8.20 E-05 |

### 4.2.4 Power and energy aspects

The aim of this section is to evaluate the mesh parameters effects from the energy and power consumption point of view. Different power consumption and efficiency indices have been tabulated in Table. 4-4. Discharge power increases by decreasing the porosity due to the larger overall collector surface that leads to a higher electric field and SCD extraction. For the very porous meshes, decreasing the wire diameter results in higher discharge power thanks to the higher curvature of the collectors. While for the low porosity meshes the wire diameter does not affect the discharge power because increasing the collector surface deteriorates the electric field intensification capability due to collectors curvature variation.

The pressure drop effect, which previously was not quantitatively obvious, has been revealed in the flow power. Since the flow power depends on pressure gradient in the domain it is clear that decreasing the porosity results in higher flow power and consequently higher pressure loss. Variation of the wire number shows different behavior for different porosities. In a very porous mesh, increasing the number of the wires results in higher flow power because the surface-friction drag and boundary layer pressure drag (as two main components of the drag force) increases by increasing the number of the wires. However, it is opposite in low porosity meshes. High diameter wires produce boundary layers

that interfere with the adjacent boundary layers due to a very low distance between the wires. The interference of the boundary layers leads to a higher boundary layer pressure drag compared to the small wires with the same porosity.

In summary, electric field efficiency decreases by increasing the porosity while fluid mechanic efficiency has a direct relationship with porosity. In addition, for very porous meshes, the lower the wire diameter, the better the electric and fluid mechanic efficiency while in low porosity meshes, the wire diameter and number variation only affect the fluid mechanic efficiency. Overall, comparing the EHD drying EHD performance numbers, very porous mesh with small wire diameter is the best option for the mesh collector configuration. Note that the electrical efficiency mostly depends on the losses arising from the plasma generation devices such as power supply, which are not included in the simulation, therefore, very high values for $\eta_E$ are indicated in the table that surely will be lower in the real case.

**Table. 4-4 Efficiency and effectiveness parameters for different mesh porosities and wire diameters**

| | $P_i$ [W] | $P_e$ [W] | $P_f$ [mW] | $\eta_E$ | $\eta_{FM}$ [mW/W] | $\eta_{Drying}$ [1/h] | $\eta_{EHD\_Drying}$ [$\times 10^3$] |
|---|---|---|---|---|---|---|---|
| Ideal Mesh | 31.06 | 30.7 | 13.70 | 0.99 | 0.45 | 0.13 | 59.0 |
| P85_N23_D1000 | 27.52 | 26.22 | 20.97 | 0.95 | 0.80 | 0.10 | 79.7 |
| P85_N46_D500 | 29.23 | 28.35 | 23.92 | 0.97 | 0.84 | 0.10 | 84.2 |
| P85_N75_D300 | 30.17 | 29.43 | 25.95 | 0.98 | 0.88 | 0.10 | 90.3 |
| P85_N97_D240 | 30.22 | 29.51 | 26.82 | 0.98 | 0.91 | 0.10 | 92.4 |
| P70_N46_D1050 | 32.16 | 31.4 | 22.89 | 0.98 | 0.73 | 0.10 | 73.4 |
| P70_N97_D500 | 31.74 | 31.14 | 22.153 | 0.98 | 0.71 | 0.10 | 70.6 |
| P50_N46_D1900 | 35.29 | 34.60 | 24.79 | 0.98 | 0.72 | 0.10 | 70.6 |
| P50_N97_D900 | 33.78 | 33.23 | 20.77 | 0.98 | 0.63 | 0.10 | 61.7 |

The electrostatic parameters and airflow velocity distribution for some selected case studies are shown in

**Fig. 4-12 Electric field distribution in the region of interest for different collector mesh porosity; a)Ideal mesh, b)85%No#23Dia1000, c)85%No#46Dia500, d)85%No#97Dia240, e)70%No#46Dia1050, f)70%No#97Dia500, g)50%No#46Dia1900, h)50%No#97Dia900, i)85%Opt4Col**
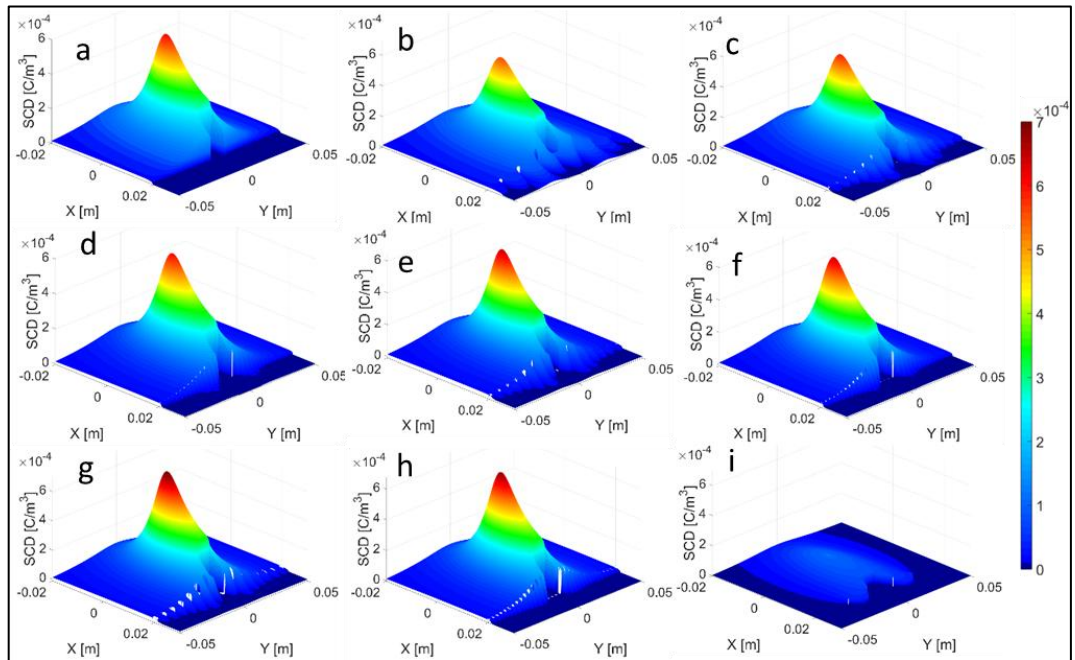


**Fig. 4-13 SCD distribution in the region of interest for different collector mesh porosity; a)Ideal mesh, b)85%No#23Dia1000, c)85%No#46Dia500, d)85%No#97Dia240, e)70%No#46Dia1050, f)70%No#97Dia500, g)50%No#46Dia1900, h) 50%No#97Dia900, i)85%Opt4Col**

**Fig. 4-14 Coulomb force distribution in the region of interest for different collector mesh porosity; a)Ideal mesh, b)85%No#23Dia1000, c)85%No#46Dia500, d)85%No#97Dia240, e)70%No#46Dia1050, f)70%No#97Dia500, g)50%No#46Dia1900, h) 50%No#97Dia900, i)85%Opt4Col**



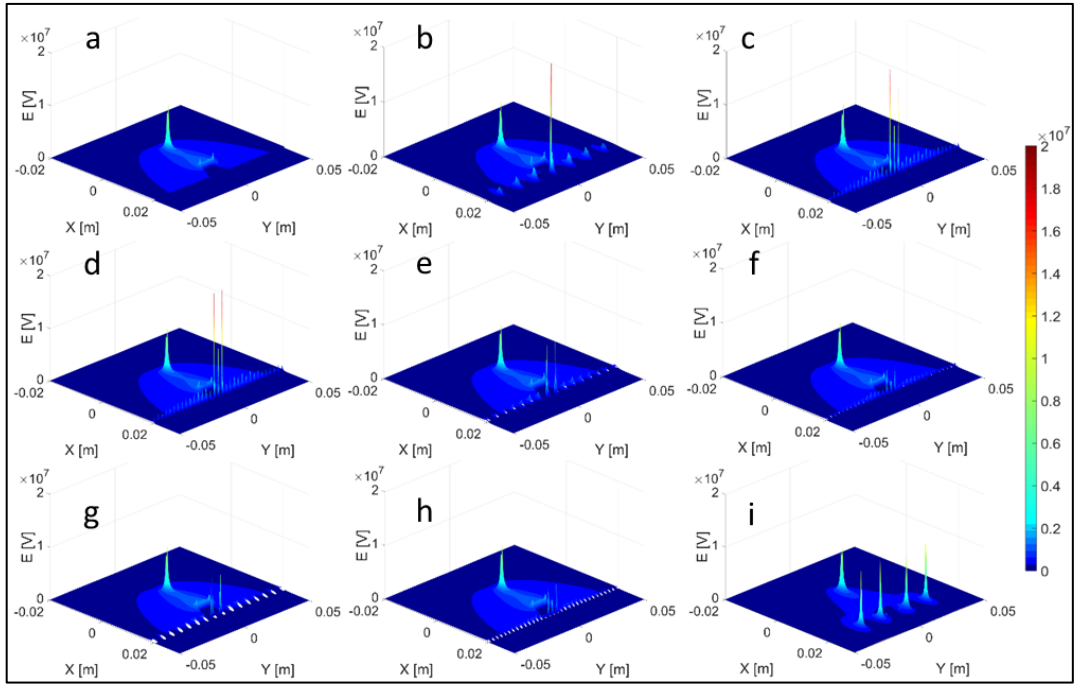**Fig. 4-15 Velocity field in the region of interest for different collector mesh porosity; a)Ideal mesh, b)85%No#23Dia1000, c)85%No#46Dia500, d)85%No#97Dia240, e)70%No#46Dia1050, f)70%No#97Dia500, g)50%No#46Dia1900, h) 50%No#97Dia900, i)85%Opt4Col**
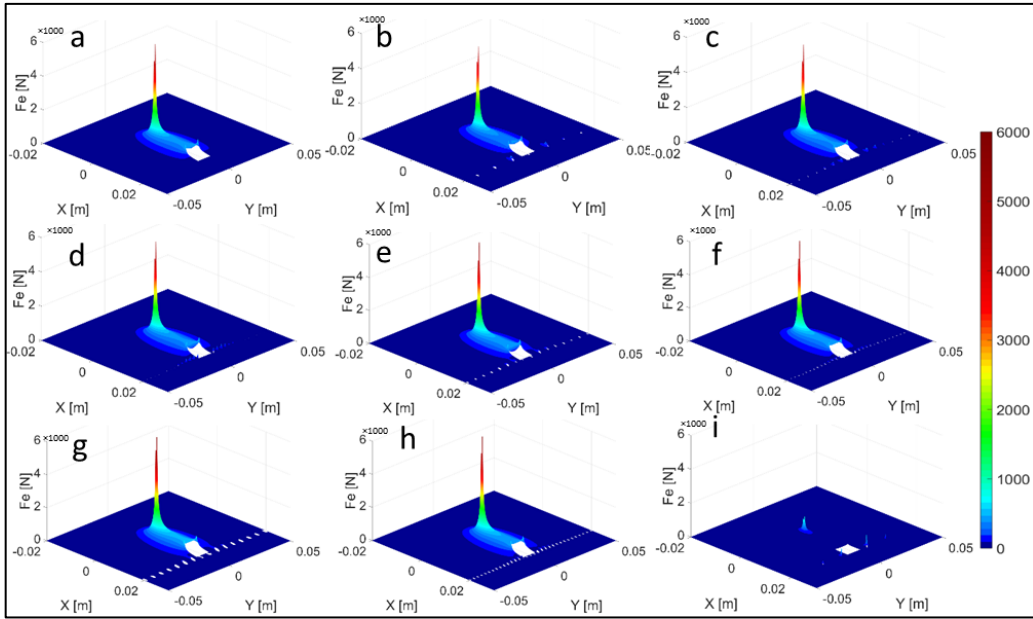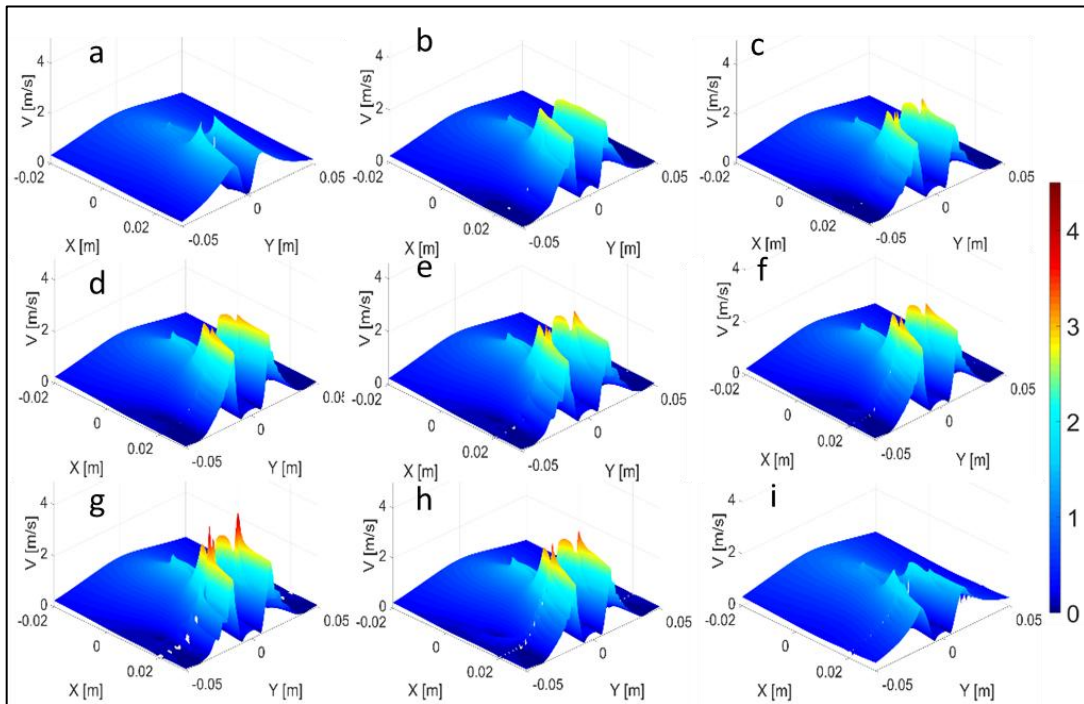
# Chapter 5: Mesh collector optimization

In this chapter attempts are made to optimize the mesh collector configuration and geometry based on the obtained information from the first section and analysis of the quantified electrostatic parameters. Finally, the optimal collector wire arrangement as a tradeoff between drying time and low energy consumption for industrial application is introduced that shows a significant improvement in terms of performance number.

## 5.1 Configurations related to mesh collector optimization

This part has been carried out to identify an optimized mesh configuration in terms of drying rate, low energy consumption and low loss generation.

Electrical power P [W] is defined as

$$P = VI \approx \boldsymbol{EJ} \approx \mu_c \rho_c E^2 \tag{54}$$

where I is ionic current which can be calculated as(Mazumder and Lai, 2018)(Shrimpton, 2009):

$$I = \left| \oiint_{\substack{emitter \\ or\ collector}} \vec{j}.d\vec{s} \right| \cong 2\pi r_{emitter} \left( \sum_i \mu_{c_i} \rho_{c_i} E \right)_{r_{emitter}} \tag{55}$$

From Eq. (54), it can be concluded that if the average value of SCD and E decreases, the power/energy consumption decreases respectively in linear and quadratic proportion.

The optimization regarding low power consumption could happen when we arrange the wires in such a way that the intensity of electric field increases close to the sample which is expected to leads to a better distribution of airflow around the sample while its average value in the domain decreases. The first challenge for this optimization is to use the lowest possible number of wires to decrease not only the average space charge density but also the average electric field in the whole domain, whereas they should be high enough close to the sample to keep the drying performance close to the ideal mesh.  In this regard, the idea of "effective distribution" refers to the increase of the Coulomb force in the region of interest; by increasing the intensity of the electric field there, and conducting the charges into that specific region. Another challenge of this optimization is to decrease the collector cross-section (diameter) as low as possible to reduce SCD, but on the other hand, for higher electric field intensity close to the sample, the collector cross-section should be high enough.

The first strategy to deal with these challenges is to only cover the length of the sample with grounded wires and the rest parts of the domain with non-conductive wires. In other words, only a few numbers of wires, which are located just behind the fruit, are activated.

The other strategy is to start with only one wire then increasing the wire number while changing their locations to find the highest electric field intensity with those wires and stop the process when the drying time is close enough to the ideal case. In this way, the lowest possible number of activated wires in the most optimal locations -in terms of high electric field intensity- will be found. However, this approach requires lots of computational effort and too many parametric sweeps. Hence, by some preliminary analytical calculations and analyzing the obtained data from the configurations related to mesh parameters study, a rough estimation about conductor wire numbers and locations can be made to reduce the computational costs. When the locations of the activated wires are found, the rest of the domain will be covered with the non-conductive wires to reach the specific desired value of porosity.

## 5.2 Optimization procedure

Based on the useful information obtained from the analysis in the previous section, in this part, the electric field has been intensified in different strategic locations by activating wires at those locations and deactivating (i.e. non-conductive wires) the rest. The strategic locations have been selected based on both the electrostatic and aerodynamic considerations. For the electrostatic aspects, firstly, the wires have been treated as charged particles and the simple electrostatic equations for the charged particles have been considered. In this way, the distance between two wires cannot be too low since the mutual electric field interaction of the wires affects the main electric field (the one between emitter and collector) so the local intensity will decrease and more wires are needed. On the other hand, if the distance becomes too high the wire cannot attract the potentially available electric field so the local electric field intensity will decrease as well. From the aerodynamic perspective, the wires should be arranged in such a way that conduct the flow towards the sample and decrease the flow separation and wake as much as possible to avoid a huge pressure loss. In addition, based on the analyses in the previous sections, the average airspeed in the domain should be high enough to obtain higher CHTC and better drying performance. Therefore, the aim was to reach almost the same airflow distribution as the ideal mesh.

Keeping in mind these two aspects, a parametric sweep study on the estimated numbers and locations has been performed. The 85% porosity case has been

selected (namely P85_N97_D240) since based the result of previous chapter it showed the best efficiency. First the activated wires number was investigated (Fig. 5-1). The rest of the domain is filled with non-conductor wires which in practice can be considered as plastic wires.
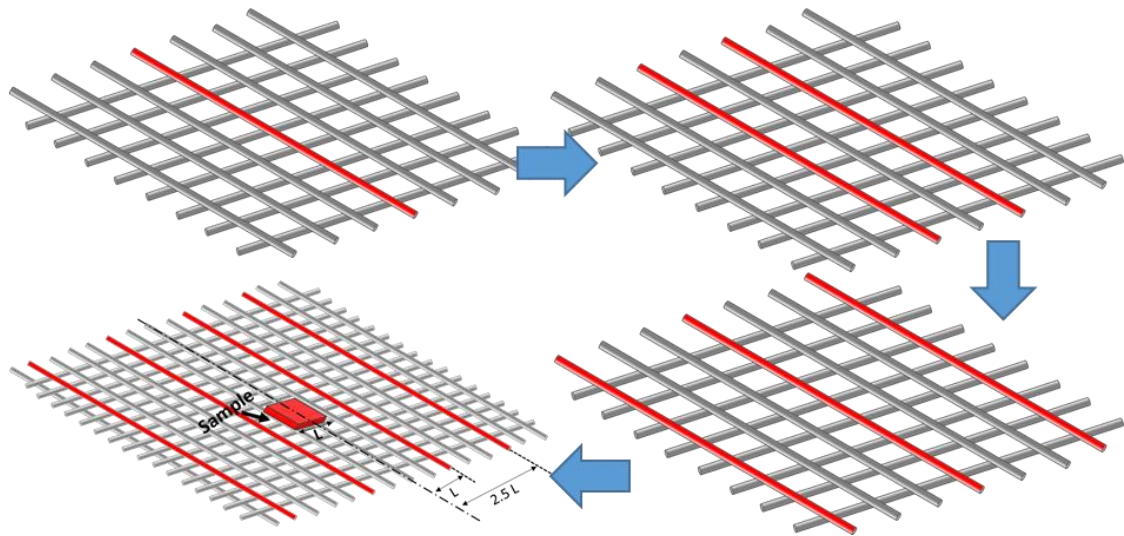


**Fig. 5-1 Schematic illustration of activation of different wires in mesh (red color stands for activated wire and gray is non-conductive wires)**

For each case a complete simulation has been performed (although very time costly for each single simulation), and EHD performance No. for each case has been evaluated. Increasing the No. of activated wires stopped when the EHD performance No. reaches to an asymptote which ends up to the EHD performance No. of all activated wires (Fig. 5-2). Comparing the EHD performance No. trend for different cases (Fig. 5-2) as well as critical drying time(Fig. 5-3) and specific energy consumption(Fig. 5-4), shows the optimal number of activated wires is 4 activated wires.
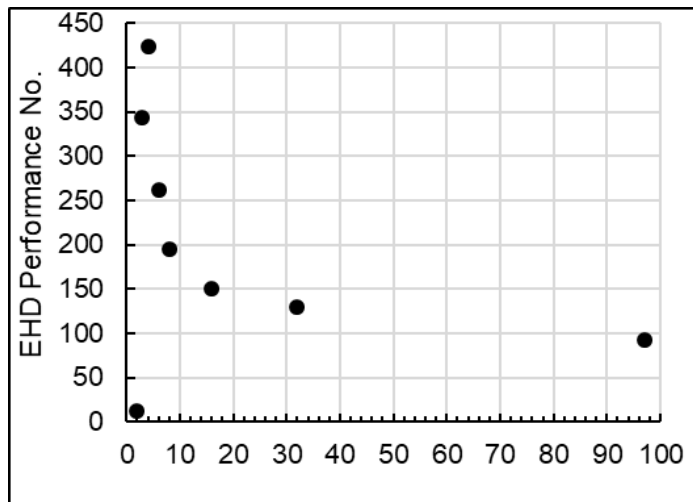
**Fig. 5-2 EHD performance No. for different activated wire numbers**
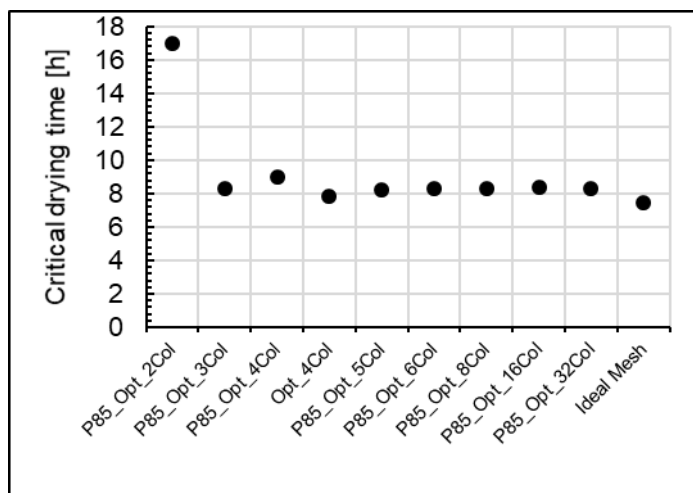


**Fig. 5-3 Critical drying time for different activated wire numbers**
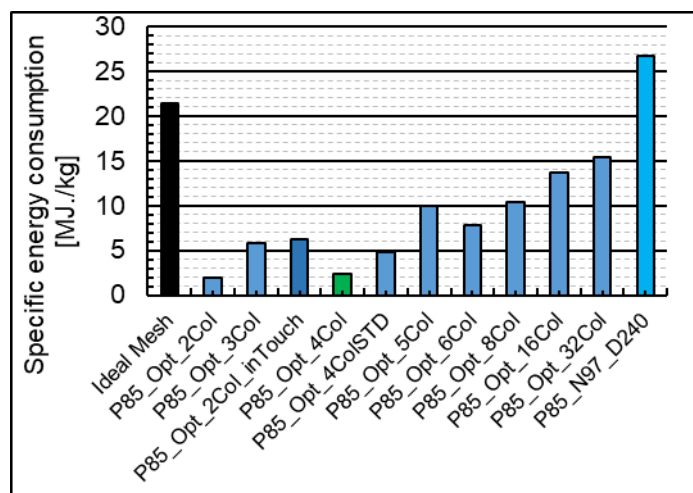


**Fig. 5-4 Specific energy consumption for different activated wire numbers**

## 5.3 The most optimized case

In the most optimized case that we could reach, 4 collector wires have been located in $\pm L_s$ and $\pm 2.5\,L_s$ from the centerline of the sample. Fig. 5-5c shows the schematic of the locations of the activated wires with respect to the sample without any non-conductive wires. As the porosity of this case (Opt_4Col) is close to 100%, it can be comparable with Ideal mesh configuration. Fig. 5-5b shows the schematics of the optimal configuration including non-conductive wires. In this case, the diameter of wires is 250µm and 90 non-conductor wires have been used to reach the porosity of 85%. Hence, this configuration (P85_Opt_4Col) is comparable with other 85% porosity configurations. As it is shown in Fig. 5-5a with only four collector wires (P85_Opt_4Col), the drying time is lower than other 85% porosity configurations (e.g. P85_N23_D1000). For the porosity of almost 100%, quite the same drying time of the Ideal mesh could be reached with Opt4Col.
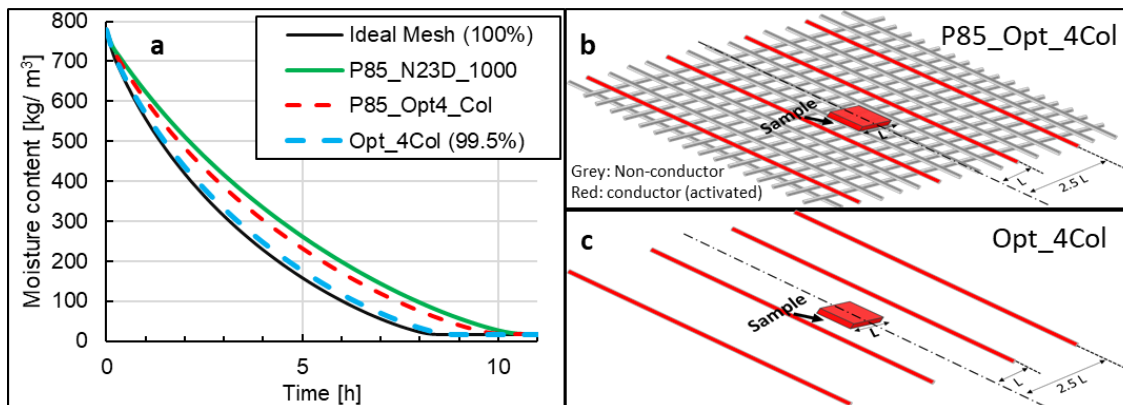


**Fig. 5-5 a) Drying curve b) optimized configuration with 4 collector (activated) wires and non-conductor wires with porosity of 85% c) optimized configuration without non-conductive wires and porosity of almost 100%**

The difference between the drying time of the ideal and optimized mesh configuration (P85_Opt_4Col), whereas they both have the same airflow distribution, is due to the pressure loss effect of the mesh porosity. This has been demonstrated in another configuration (Opt_4Col), where all the non-conductor wires of P85_Opt_4Col case have been removed to reach the porosity of almost 100%. The results obviously show the mesh pressure loss effect on the drying rate, since the critical drying time of Opt4Col configuration is almost similar to the ideal mesh configuration (Table. 5-1).

**Table. 5-1 Quantitative evaluation of the most important parameters for comparing optimal configuration with other configurations**

| | Porosity [%] | $t_{crit}$ [h] | Average CHTC [W/m²K] | Maximum Airspeed [m/s] | Average Airspeed* [m/s] | Average $F_e$* [N] | Average E* [kV] | Average SCD* [C/m³]×10⁵ |
|---|---|---|---|---|---|---|---|---|
| Ideal Mesh | 100 | 7.47 | 37.49 | 2.32 | 0.67 | 20.29 | 255 | 7.96 |
| P85_N23_Dia1000 | 85 | 9.56 | 19.83 | 2.78 | 0.56 | 20.73 | 256 | 8.10 |
| P85_Opt_2Col | 85 | 17.01 | 8.34 | 0.57 | 0.11 | 1.33 | 142 | 0.93 |
| P85_Opt_3Col | 85 | 8.20 | 27.80 | 2.63 | 0.60 | 4.90 | 180 | 2.71 |
| P85_Opt_4Col | 85 | 9.03 | 25.23 | 2.02 | 0.67 | 5.07 | 195 | 2.60 |
| Opt_4Col | 99.5 | 7.84 | 33.68 | 2.01 | 0.61 | 5.07 | 195 | 2.60 |
| P85_Opt_4ColSTD | 85 | 8.33 | 27.30 | 2.66 | 0.60 | 4.54 | 181 | 2.51 |
| P85_Opt_5Col | 85 | 8.22 | 27.71 | 2.63 | 0.60 | 7.89 | 206 | 3.81 |
| P85_Opt_6Col | 85 | 8.33 | 27.30 | 2.66 | 0.60 | 7.38 | 208 | 3.54 |
| P85_Opt_8Col | 85 | 8.31 | 27.38 | 2.54 | 0.60 | 10.59 | 233 | 4.55 |
| P85_Opt_16Col | 85 | 8.35 | 27.16 | 2.67 | 0.60 | 15.63 | 259 | 6.03 |
| P85_Opt_32Col | 85 | 8.32 | 27.57 | 2.64 | 0.60 | 17.69 | 255 | 6.94 |

*in the region of interest

The difference in electrostatic values between the optimized case and the other studied configurations is well obvious in Fig. 5-6. The electric field intensity distribution in P85_N23_D1000 is very high close to the drying matter that generates a higher maximum airspeed but the intensity decreases in the rest of the domain that results in lower average velocity (Fig. 5-6d). In the optimized case (P85_Opt_4Col), the electric field is equally intensified close to the sample as well as far from the sample, to reach a good flow distribution around the drying matter and high average airspeed, at the same time, while keeping the average electric field intensity very low(Table. 5-1). It is noteworthy to mention that, attempts have been made to more intensify the electric field close to the sample by increasing the diameter of the two collectors, which were located close to the sample, but it did not end up in a better drying rate. Moreover, exactly opposite to the previous attempt, increasing the intensity far from the sample in order to affect the average airspeed, has failed too. Therefore, the most optimized electric field intensity distribution has been considered as equally distributed electric intensity on collectors.
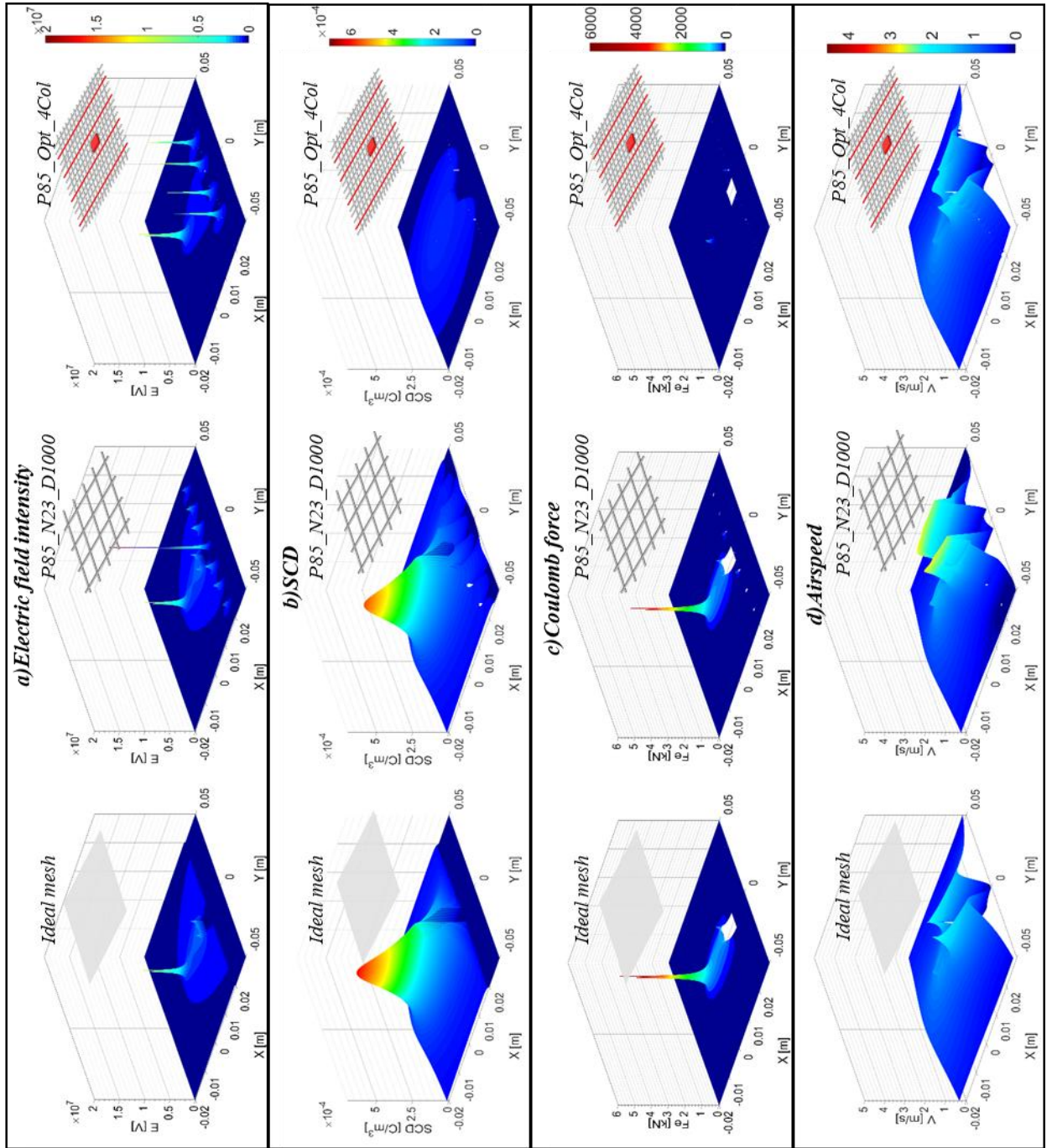
**Fig. 5-6 Distribution of electrostatic parameters and resulting airspeed in the region of interest**

As it is clear from Table. 5-2, although the optimized case (P85_Opt_4Col), consumes a very low input power, but due to low discharge power, the electrical efficiency is similar to the other cases. In addition, the drying efficiency has been improved compared to the non-ideal/non-optimized meshes because of effective flow distribution around the sample.

**Table. 5-2 Efficiency and effectiveness parameters for comparing optimal configuration with other configurations**

| | $P_i$ [W] | $P_e$ [W] | $P_f$ [mW] | $\eta_E$ | $\eta_{FM}$ [mW/W] | $\eta_{Drying}$ [1/h] | $\eta_{EHD\_Drying}$ [×10³] |
|---|---|---|---|---|---|---|---|
| Ideal Mesh | 31.06 | 30.7 | 13.70 | 0.99 | 0.45 | 0.13 | 59.0 |
| P85_N23_D1000 | 27.52 | 26.22 | 20.97 | 0.95 | 0.80 | 0.10 | 79.7 |
| P85_N46_D500 | 29.23 | 28.35 | 23.92 | 0.97 | 0.84 | 0.10 | 84.2 |
| P85_N75_D300 | 30.17 | 29.43 | 25.95 | 0.98 | 0.88 | 0.10 | 90.3 |
| P85_N97_D240 | 30.22 | 29.51 | 26.82 | 0.98 | 0.91 | 0.10 | 92.4 |
| P70_N46_D1050 | 32.16 | 31.4 | 22.89 | 0.98 | 0.73 | 0.10 | 73.4 |
| P70_N97_D500 | 31.74 | 31.14 | 22.153 | 0.98 | 0.71 | 0.10 | 70.6 |
| P50_N46_D1900 | 35.29 | 34.60 | 24.79 | 0.98 | 0.72 | 0.10 | 70.6 |
| P50_N97_D900 | 33.78 | 33.23 | 20.77 | 0.98 | 0.63 | 0.10 | 61.7 |
| P85_Opt_4Col | 2.9 | 2.64 | 20.40 | 0.91 | 7.73 | 0.11 | 773.8 |
| P85_Opt_3Col | 8.16 | 7.28 | 21.64 | 0.89 | 2.97 | 0.13 | 343.6 |
| P85_Opt_2Col_inTouch | 7.54 | 6.78 | 21.67 | 0.90 | 3.20 | 0.13 | 374.4 |
| P85_Opt_5Col | 13.09 | 11.0 | 21.67 | 0.84 | 1.97 | 0.13 | 215.1 |
| P85_Opt_2Col | 1.24 | 1.074 | 0.27 | 0.87 | 0.25 | 0.06 | 13.0 |
| P85_Opt_6Col | 10.10 | 9.02 | 22.13 | 0.89 | 2.45 | 0.12 | 261.7 |
| P85_Opt_8Col | 13.56 | 12.26 | 22.10 | 0.90 | 1.80 | 0.12 | 194.4 |
| P85_Opt_16Col | 17.81 | 16.34 | 22.25 | 0.92 | 1.36 | 0.12 | 150.1 |
| P85_Opt_32Col | 20.14 | 18.52 | 21.79 | 0.92 | 1.18 | 0.12 | 130.3 |
| P85_Opt_4ColSTD | 6.27 | 5.45 | 22.13 | 0.87 | 4.06 | 0.12 | 423.9 |

The superiority of such a configuration over others appears in the fluid mechanic efficiency index, which is almost 10 times higher than other cases. Looking at average Coulomb force provided in Table. 5-1 and its distribution in Fig. 5-6c, reveals that with almost 4 times lower force, quite the same average airspeed and the airspeed distribution of Ideal mesh are obtained (Fig. 5-6d). The point here is that as the momentum transfer between ions and neutral air particles occurs with low efficiency, after a certain point increasing the number of ions (SCD) in the region does not help to have a very higher average airspeed. The

closed drying chamber and mesh porosity could be other factors which do not allow having higher average airspeed. So, for this specific configuration under study, having an average $F_e$ about 5.1 [N] is enough for generating average airspeed of 0.67 [m/s] if and only if this force is effectively distributed to conduct the airflow properly. The higher values of $F_e$ just increase the fluid mechanic losses without any other benefits.

All these improvements result in a striking difference in EHD performance number compared to other mesh collector configurations, which explicitly shows the impact of effective electric field intensification distribution around the sample.

Small collector surface leads to lower SCD compare to the other configurations (Fig. 5-6 and Table. 5-1). Low SCD in EHD drying, in addition to the less toxic gas emission, reduces the electric charge barrier on the surface of the drying mater which helps to reach a better drying rate in EHD drying technologies. The dissimilarity of the SCD and electric field distributions in different configurations results in an obvious difference in Coulomb force distribution between the optimized case and the other configurations. However, due to the effective distribution of this low amount force, almost the same ideal airflow distribution and average airspeed, have been reached by the optimized configuration.

If we only consider the energy consumption of the optimal configuration during the drying time ($P_i \times t_{crit}$), it is almost 10 times lower than other configurations. This is a huge improvement and step towards more efficient EHD drying device. This configuration can be proposed for further experimental validations.
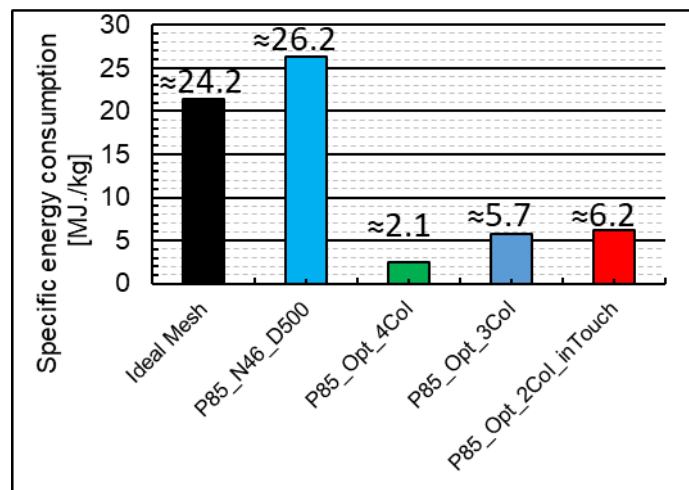


**Fig. 5-7 Specific energy consumption of optimal configuration vs. other configurations**

**Conclusion**

The fully coupled, conjugate continuum EHD drying process of a food product with wire to mesh configuration, was investigated numerically. In particular, two aims were considered: 1) to evaluate collector mesh porosity effect as a step towards a more realistic model; 2) to employ the effective electric field intensification concept in order to reach an optimum collector mesh configuration. To this end, the major driving parameters such as Coulomb force, electric field, and space charge density, have been quantified, represented and analyzed. The results of this study lead to the following conclusions:

In the wire to mesh configuration, although decreasing the porosity of the mesh results in a higher pressure drop, since the mesh wires are collector electrodes as well, the dehydration kinetics remains almost the same with a penalty of higher energy consumption. Hence, depending on the fruit slice size, it is possible to change the mesh porosity without affecting the drying time.

A comprehensive performance index for EHD drying devices has been introduced. EHD performance number includes evaluation of all the individual major sub-processes and gives an overall efficiency analysis of the device, that facilitates the comparison between different configurations. Different EHD sub-processes have been analyzed and discussed by the new index that clearly showed the advantages of this tool in gaining a deeper insight into the underlying physics of the EHD-drying process.

This research demonstrated that by having a proper analysis of the electric field and airflow distribution, it is possible to reach an optimal configuration of the collector wires, in which the electric field is intensified in a few certain locations that ends up to an ideal distribution of airflow (i.e. as in ideal mesh) around the drying matter. Then based on this kind of analyses, an optimal configuration has been introduced that despite of operating with very low energy consumption, shows a better drying performance in terms of drying time, compared to the other mesh configurations.

# Bibliography

Ahmed, N. *et al.* (2013) *Different Drying Methods: Their Applications and Recent Advances*, *Int. J. Food Nutr. Saf.* Available at: https://www.researchgate.net/publication/297759340 (Accessed: 13 June 2019).

Alem-Rajabif, A. and Lai, F. C. (2005) 'EHD-Enhanced Drying of Partially Wetted Glass Beads', *Drying Technology*, 23(3), pp. 597–609. doi: 10.1081/DRT-200054150.

Annand, W. J. D. (2016) 'The Resistance to Air Flow of Wire Gauzes', *Journal of the Royal Aeronautical Society*, 57(507), pp. 141–146. doi: 10.1017/s036839310013007x.

Aregawi, W. *et al.* (2013) 'Dehydration of apple tissue: Intercomparison of neutron tomography with numerical modelling', *International Journal of Heat and Mass Transfer*. Elsevier Ltd, 67, pp. 173–182. doi: 10.1016/j.ijheatmasstransfer.2013.08.017.

Bajgai, T. R. *et al.* (2006) 'Electrohydrodynamic drying - A concise overview', *Drying Technology*, 24(7), pp. 905–910. doi: 10.1080/07373930600734091.

Barthakur, N. . (1989) 'AN ELECTROSTATIC METHOD OF DRYING SALINE WATER', *Drying Technology*, 7(3), pp. 503–521. doi: 10.1080/07373938908916606.

Barthakur, N. N. and AL-Kanani, T. (1990) 'An electrohydrodynamic technique for removal of moisture from soil samples', *Communications in Soil Science and Plant Analysis*. Taylor & Francis Group , 21(7–8), pp. 649–665. doi: 10.1080/00103629009368260.

Barthakur, N. N. and Bhartendu, S. (1988) 'Enhancement of evaporation rates from thin layers of liquids exposed to air ions', *International Journal of Biometeorology*. Springer-Verlag, 32(3), pp. 163–167. doi: 10.1007/BF01045274.

Basiry, M. and Esehaghbeygi, A. (2010) 'Electrohydrodynamic (EHD) drying of rapeseed (Brassica napus L.)', *Journal of Electrostatics*. Elsevier, 68(4), pp. 360–363. doi: 10.1016/J.ELSTAT.2010.05.002.

Bastien, F. (1987) 'Acoustics and gas discharges: applications to loudspeakers', *Journal of Physics D: Applied Physics*, 20(12), pp. 1547–1557. doi: 10.1088/0022-3727/20/12/001.

Brundrett, E. (1993) 'Prediction of Pressure Drop for Incompressible Flow Through Screens', *Journal of Fluids Engineering*, 115(2), p. 239. doi: 10.1115/1.2910130.

Burgreen, D. and Nakache, F. R. (1964) 'Electrokinetic Flow in Ultrafine Capillary Slits 1', *The Journal of Physical Chemistry*, 68(5), pp. 1084–1091. doi: 10.1021/j100787a019.

Cao, W., Nishiyama, Y. and Koide, S. (2004) 'Electrohydrodynamic drying characteristics of wheat using high voltage electrostatic field', *Journal of Food Engineering*. Elsevier, 62(3), pp. 209–213. doi: 10.1016/S0260-8774(03)00232-2.

Casey, M. and Wintergerste, T. (2000) *Special Interst Group on 'Quality and Trust in Industrial CFD' Best Practice Guidelines*. First edit. ERCOFTAC.

CASTELLANOS, A. (2008) *ELECTROHYDRODYNAMICS, Evolution*.

Çetin, B. and Li, D. (2011) 'Dielectrophoresis in microfluidics technology', *ELECTROPHORESIS*, 32(18), pp. 2410–2427. doi: 10.1002/elps.201100167.

Chakraborty, S. (2006) 'Analytical solutions of Nusselt number for thermally fully developed flow in microtubes under a combined action of electroosmotic forces and imposed pressure gradients', *International Journal of Heat and Mass Transfer*, 49(3–4), pp. 810–813. doi: 10.1016/j.ijheatmasstransfer.2005.07.048.

Chakraborty, S. (2014) 'Electrocapillary', in *Encyclopedia of Microfluidics and Nanofluidics*. Boston, MA: Springer US, pp. 1–15. doi: 10.2307/24940724.

Chen, Y. H. and Barthakur, N. N. (1991) 'Potato slab dehydration by air ions from corona discharge', *International Journal of Biometeorology*. Springer-Verlag, 35(2), pp. 67–70. doi: 10.1007/BF01087479.

CHRISTENSON, E. A. and MOLLER, P. S. (1967) 'Ion-neutral propulsion in atmospheric media.', *AIAA Journal*, 5(10), pp. 1768–1773. doi: 10.2514/3.4302.

Corke, T. *et al.* (2002) 'Application of weakly-ionized plasmas as wing flow-control devices', in *40th AIAA Aerospace Sciences Meeting & Exhibit*. Reston, Virigina: American Institute of Aeronautics and Astronautics. doi: 10.2514/6.2002-350.

Curcio, S. *et al.* (2016) 'Formulation of a 3D conjugated multiphase transport model to predict drying process behavior of irregular-shaped vegetables', *Journal of Food Engineering*, 1(176), pp. 36–55. Available at: https://www.sciencedirect.com/science/article/pii/S0260877415300662 (Accessed: 17 June 2019).

Defraeye, T. (2014) 'Advanced computational modelling for drying processes - A review', *Applied Energy*, 131, pp. 323–344. doi: 10.1016/j.apenergy.2014.06.027.

Defraeye, T., Blocken, B. and Carmeliet, J. (2010) 'CFD analysis of convective heat transfer at the surfaces of a cube immersed in a turbulent boundary layer', *International Journal of Heat and Mass Transfer*. Elsevier Ltd, 53(1–3), pp. 297–308. doi: 10.1016/j.ijheatmasstransfer.2009.09.029.

Defraeye, T., Blocken, B. and Carmeliet, J. (2011) 'Analysis of convective heat and mass transfer coefficients for convective drying of a porous flat plate by conjugate modelling', *International Journal of Heat and Mass Transfer*, 15(55), pp. 112–24. doi: 10.1016/j.ijheatmasstransfer.2011.08.047.

Defraeye, T., Blocken, B. and Carmeliet, J. (2012) 'Analysis of convective heat and mass transfer coefficients for convective drying of a porous flat plate by conjugate modelling', *International Journal of Heat and Mass Transfer*. Elsevier Ltd, 55(1–3), pp. 112–124. doi: 10.1016/j.ijheatmasstransfer.2011.08.047.

Defraeye, T. and Martynenko, A. (2018) 'Electrohydrodynamic drying of food: New insights from conjugate modeling', *Journal of Cleaner Production*. Elsevier Ltd, 198, pp. 269–284. doi: 10.1016/j.jclepro.2018.06.250.

Defraeye, T. and Martynenko, A. (2019) 'Electrohydrodynamic drying of multiple food products: Evaluating the potential of emitter-collector electrode configurations for upscaling', *Journal of Food Engineering*. Elsevier, 240(July 2018), pp. 38–42. doi: 10.1016/j.jfoodeng.2018.07.011.

Defraeye, T. and Verboven, P. (2017) 'Convective drying of fruit: Role and impact of moisture transport properties in modelling', *Journal of Food Engineering*. Elsevier Ltd, 193, pp. 95–107. doi: 10.1016/j.jfoodeng.2016.08.013.

Defraeye, T., Verboven, P. and Nicolai, B. (2013) 'CFD modelling of flow and scalar exchange of spherical food products: Turbulence and boundary-layer modelling', *Journal of Food Engineering*. Elsevier Ltd, 114(4), pp. 495–504. doi: 10.1016/j.jfoodeng.2012.09.003.

Faraday, M. (1830) 'Experimental Researches in Electricity.', *Proceedings of the Royal Society of London*, 3(0), pp. 91–93. doi: 10.1098/rspl.1830.0051.

Fylladitakis, E. D., Theodoridis, M. P. and Moronis, A. X. (2014) 'Review on the history, research, and applications of electrohydrodynamics', *IEEE Transactions on Plasma Science*, 42(2), pp. 358–375. doi: 10.1109/TPS.2013.2297173.

Ghazanchaei, M., Adamiak, K. and Castle, G.S. Peter (2015) 'Predicted flow characteristics of a wire-nonparallel plate type electrohydrodynamic gas pump using the Finite Element Method', *Journal of Electrostatics*, 73, pp. 103–111. doi: 10.1016/j.elstat.2014.11.003.

Ghazanchaei, M., Adamiak, K. and Castle, G. S Peter (2015) 'Predicted flow characteristics of a wire-nonparallel plate type electrohydrodynamic gas pump using the Finite Element Method', *Journal of Electrostatics*. Elsevier Ltd, 73, pp. 103–111. doi: 10.1016/j.elstat.2014.11.003.

Goldman, M. and Goldman, A. (1978) 'Corona Discharges', in Hirsch, M. N. and Oksam, H. J. (eds) *Gaseous electronics - Volume 1: Electrical Discharges*. New York: Academic Press Inc., pp. 219–290. doi: 10.1016/B978-0-12-349701-7.50009-2.

Halder, A. and Datta, A. K. (2012) 'Surface heat and mass transfer coefficients for multiphase porous media transport models with rapid evaporation', *Food and Bioproducts Processing*, 90(3), pp. 475–490. doi: 10.1016/j.fbp.2011.10.005.

Hashinaga, F. *et al.* (1999) 'ELECTROHYDRODYNAMIC (EHD) DRYING OF APPLE SLICES', *Drying Technology*. Taylor & Francis Group , 17(3), pp. 479–495. doi: 10.1080/07373939908917547.

Hunter, R. J. (2013) 'Zeta potential in colloid science : principles and applications', p. 386. Available at: https://books.google.ch/books?hl=en&lr=&id=9I3-BAAAQBAJ&oi=fnd&pg=PP1&dq=Zeta+potential+in+colloid+science+principles+and+applications&ots=EWV-K7PsVt&sig=wIG4wvInAkSfDD3FBDUUFgqvivw#v=onepage&q=Zeta potential in colloid science principles and applications (Accessed: 1 July 2019).

Hwang, G. *et al.* (2011) 'Electro-osmotic propulsion of helical nanobelt swimmers', *The International Journal of Robotics Research*, 30(7), pp. 806–819. doi: 10.1177/0278364911407231.

Iranshahi, K. and Mani, M. (2018) 'Dielectric Barrier Discharge Actuators Employed as Alternative to Conventional High-Lift Devices', *Journal of Aircraft*. American Institute of Aeronautics and Astronautics, 55(5), pp. 1–10. doi: 10.2514/1.C034690.

Jayaraman, K. S. and Das Gupta, D. K. (1992) 'DEHYDRATION OF FRUITS AND VEGETABLES - RECENT DEVELOPMENTS IN PRINCIPLES AND TECHNIQUES', *Drying Technology*. Taylor & Francis Group , 10(1), pp. 1–50. doi: 10.1080/07373939208916413.

Jewell-Larsen *et al.* (2008) 'Modeling of corona-induced electrohydrodynamic flow with COMSOL multiphysics', in *ESA Annual Meeting on Electrostatics, Minneapolis*, pp. 17–19. Available at: http://citeseerx.ist.psu.edu/viewdoc/download?doi=10.1.1.452.6900&rep=rep1&type=pdf (Accessed: 26 December 2018).

Johnson, M. J. and Go, D. B. (2017) 'Recent advances in electrohydrodynamic pumps operated by ionic winds: a review', *Plasma Sources Science and Technology*. IOP Publishing, 26(10), p. 103002. doi: 10.1002/ardp.19322700106.

Kibler, K. G. and Carter, H. G. (1974) 'Electrocooling in gases', *Journal of Applied Physics*, 45(10), pp. 4436–4440. doi: 10.1063/1.1663069.

Kocik, M. *et al.* (2009) 'Particle image velocimetry measurements of wire-nonparallel plates type electrohydrodynamic gas pump', *IEEE Transactions on Dielectrics and Electrical Insulation*, 16(2), pp. 312–319. doi: 10.1109/TDEI.2009.4815158.

Kriegseis, J. *et al.* (2013) 'On the classification of dielectric barrier discharge plasma actuators: A comprehensive performance evaluation study', *Journal of Applied Physics*, 114(5), p. 053301. doi: 10.1063/1.4817366.

Krueger, A. P., Hicks, W. W. and Beckett, J. C. (1958) 'Effects of unipolar air ions on microorganisms and on evaporation', *Journal of the Franklin Institute*. Pergamon, 266(1), pp. 9–19. doi: 10.1016/0016-0032(58)90803-2.

Kudra, T. and Martynenko, A. (2015) 'Energy Aspects in Electrohydrodynamic Drying', *Drying Technology*, 33(13), pp. 1534–1540. doi: 10.1080/07373937.2015.1009540.

Kudra, T. and Mujumdar, A. S. (2009) *Advanced Drying Technologies, 2nd Edition*. CRC Press. doi: 10.1201/9781420073898.

Lai, F. C. (2010) 'A prototype of EHD-enhanced drying system', *Journal of Electrostatics*. doi: 10.1016/j.elstat.2009.08.002.

Lai, F. C. and Lai, K.-W. (2002) 'Ehd-Enhanced Drying With Wire Electrode', *Drying Technology*, 20(7), pp. 1393–1405. doi: 10.1081/DRT-120005858.

Lai, F. C. and Sharma, R. K. (2005) 'EHD-enhanced drying with multiple needle electrode', *Journal of Electrostatics*. doi: 10.1016/j.elstat.2004.10.004.

Lai, F. C. and Wong, D. S. (2003) 'EHD-Enhanced Drying with Needle Electrode', *Drying Technology*. Taylor & Francis Group , 21(7), pp. 1291–1306. doi: 10.1081/DRT-120023181.

Laws, E. M. and Livesey, J. L. (1978) *FLOW THROUGH SCREENS, Ann. Rev. Fluid Mech*. Available at: www.annualreviews.org (Accessed: 10 May 2019).

Lee, P. D., Quested, P. N. and McLean, M. (1998) 'Modelling of Marangoni effects in electron beam melting', *Philosophical Transactions of the Royal Society of London. Series A: Mathematical, Physical and Engineering Sciences*. Edited by E. D. Hondros, M. McLean, and K. C. Mills, 356(1739), pp. 1027–1043. doi: 10.1098/rsta.1998.0207.

MacCurdy, R. and Hod, L. (2016) 'System and methods for actuation using electro-osmosis'. U.S.: U.S. Patent and Trademark Office. Available at: https://patents.google.com/patent/US9487387B2/en (Accessed: 29 June 2019).

Martynenko, A. *et al.* (2017) 'Driving forces for mass transfer in electrohydrodynamic (EHD) drying', *Innovative Food Science and Emerging Technologies*. Elsevier, 43(May), pp. 18–25. doi: 10.1016/j.ifset.2017.07.022.

Martynenko, A. and Kudra, T. (2016a) 'Electrically-induced transport phenomena in EHD drying - A review', *Trends in Food Science and Technology*. Elsevier Ltd, 54, pp. 63–73. doi: 10.1016/j.tifs.2016.05.019.

Martynenko, A. and Kudra, T. (2016b) 'Electrohydrodynamic (EHD) drying of grape pomace', *Japan Journal of Food Engineering*, 17(4), pp. 123–129. doi: 10.11301/jsfe.17.123.

Martynenko, A., Kudra, T. and Yue, J. (2017) 'Multipin EHD dryer: Effect of electrode geometry on charge and mass transfer', *Drying Technology*. Taylor & Francis, 35(16), pp. 1970–1980. doi: 10.1080/07373937.2017.1285311.

Martynenko, A. and Zheng, W. (2016) 'Electrohydrodynamic drying of apple slices: Energy and quality aspects', *Journal of Food Engineering*. Elsevier Ltd, 168, pp. 215–222. doi: 10.1016/j.jfoodeng.2015.07.043.

Matsunuma, T. and Segawa, T. (2013) 'Active Control of Tip Leakage Flow for Low-Pressure Turbine by Ring-Type Plasma Actuators', in *43rd Fluid Dynamics Conference*. Reston, Virginia: American Institute of Aeronautics and Astronautics. doi: 10.2514/6.2013-2726.

Mazumder, A. K. M. M. H. and Lai, F. C. (2018) 'Enhancement of Forced Convection Using a Two-Stage Electrohydrodynamic Gas Pump', *Journal of Thermophysics and Heat Transfer*, 32(3), pp. 617–626. doi: 10.2514/1.T5345.

Melcher, J. R. and Taylor, G. I. (1969) 'Electrohydrodynamics: A Review of the Role of Interfacial Shear Stresses', *Annual Review of Fluid Mechanics*. Annual Reviews 4139 El Camino Way, P.O. Box 10139, Palo Alto, CA 94303-0139, USA , 1(1), pp. 111–146. doi: 10.1146/annurev.fl.01.010169.000551.

Meroth, A. M. *et al.* (1999) 'Numerical solution of nonstationary charge coupled problems', *Journal of Electrostatics*, 45(3), pp. 177–198. doi: 10.1016/S0304-3886(98)00046-1.

Misra, N. N. *et al.* (2018) 'Thermodynamics, transport phenomena, and electrochemistry of external field-assisted nonthermal food technologies', *Critical Reviews in Food Science and Nutrition*, 58(11), pp. 1832–1863. doi: 10.1080/10408398.2017.1287660.

Moatimid, G. M. and Hassan, M. A. (2013) 'The Instability of an Electrohydrodynamic Viscous Liquid Micro-Cylinder Buried in a Porous Medium: Effect of Thermosolutal Marangoni Convection', *Mathematical Problems in Engineering*, 2013, pp. 1–14. doi: 10.1155/2013/416562.

Mujumdar, A. S. and Jangam, S. V (2011) 'Some Innovative Drying Technologies for Dehydration of Foods', in *ICEF*. Athens, Greece, pp. 555–556. Available at: http://www.serve.me.nus.edu.sg/arun.

Mujumdar, A. S. and Mashelkar, R. A. (2013) *Advances in transport processes. IX*.

Ohyama, R., Inoue, K. and Chang, J. S. (2007) 'Schlieren optical visualization for transient EHD induced flow in a stratified dielectric liquid under gas-phase ac corona discharges', *Journal of Physics D: Applied Physics*, 40(2), pp. 573–578. doi: 10.1088/0022-3727/40/2/036.

Ongkodjojo Ong, A., Abramson, A. R. and Tien, N. C. (2014) 'Electrohydrodynamic Microfabricated Ionic Wind Pumps for Thermal Management Applications', *Journal of Heat Transfer*. American Society of Mechanical Engineers, 136(6), p. 061703. doi: 10.1115/1.4026807.

Ould Ahmedou, S. A., Rouaud, O. and Havet, M. (2009) 'Assessment of the Electrohydrodynamic Drying Process', *Food and Bioprocess Technology*. Springer-Verlag, 2(3), pp. 240–247. doi: 10.1007/s11947-008-0078-6.

Ould Ahmedou, S. and Havet, M. (2009) 'Effect of process parameters on the EHD airflow', *Journal of Electrostatics*. Elsevier Ltd, 67(2–3), pp. 222–227. doi: 10.1016/j.elstat.2009.01.055.

Oussalah, N. and Zebboudj, Y. (2006) 'Finite-element analysis of positive and negative corona discharge in wire-to-plane system', *The European Physical Journal Applied Physics*, 34, pp. 215–223. doi: 10.1051/epjap:2006063.

P, C., MV, D. B. and G, R. (2016) 'Conjugate heat and mass transfer in drying: A modeling review', *Journal of Food Engineering.*, 1(176), pp. 28–35. Available at: https://www.sciencedirect.com/science/article/pii/S0260877415003842 (Accessed: 17 June 2019).

Phung, T. H., Oh, S. and Kwon, K.-S. (2018) 'High-resolution Patterning Using Two Modes of Electrohydrodynamic Jet: Drop on Demand and Near-field Electrospinning', *Journal of Visualized Experiments*, (137), p. e57846. doi: 10.3791/57846.

Podlinski, J. *et al.* (2013) 'Pumping Effect Measured by PIV Method in a Multilayer Spike Electrode EHD Device for Air Cleaning', *IEEE Transactions on Industry Applications*, 49(6), pp. 2402–2408. doi: 10.1109/TIA.2013.2265214.

Radu, I., Bartnikas, R. and Wertheimer, M. R. (2003) 'Dielectric barrier discharges in helium at atmospheric pressure: experiments and model in the needle-plane geometry', *Journal of Physics D: Applied Physics*, 36(11), pp. 1284–1291. doi: 10.1088/0022-3727/36/11/308.

Robinson, M. (1961) 'Movement of air in the electric wind of the corona discharge', *Transactions of the American Institute of Electrical Engineers, Part I: Communication and Electronics*, 80(2), pp. 143–150. doi: 10.1109/TCE.1961.6373091.

Roth, J., Sherman, D. and Wilkinson, S. (1998) 'Boundary layer flow control with a one atmosphere uniform glow discharge surface plasma', in *36th AIAA Aerospace Sciences Meeting and Exhibit*. Reston, Virigina: American Institute of Aeronautics and Astronautics. doi: 10.2514/6.1998-328.

Saneewong Na Ayuttaya, S. *et al.* (2012) 'Effect of Ground Arrangements on Swirling Flow in a Rectangular Duct Subjected to Electrohydrodynamic Effects', *Journal of Fluids Engineering*, 134(5), p. 051211. doi: 10.1115/1.4006699.

Sheu, T. W. H., Kuo, S. H. and Lin, R. K. (2012) 'Prediction of a temperature-dependent electroosmotically driven microchannel flow with the Joule heating effect', *International Journal of Numerical Methods for Heat & Fluid Flow*, 22(5), pp. 554–575. doi: 10.1108/09615531211231244.

Shooshtari, A., Ohadi, M. and Franca, F. H. R. (2003) 'Experimental and numerical analysis of electrohydrodynamic enhancement of heat transfer in air laminar channel flow', in *Ninteenth Annual IEEE Semiconductor Thermal Measurement and Management Symposium,*. IEEE, pp. 48–52. doi: 10.1109/STHERM.2003.1194338.

Shrimpton, J. (2009) *Charge Injection Systems*, *Physiological Research*. Berlin, Heidelberg: Springer Berlin Heidelberg (Heat and Mass Transfer). doi: 10.1007/978-3-642-00294-6.

Singh, A. *et al.* (2015) 'Electrohydrodynamic drying (EHD) of wheat and its effect on wheat protein conformation', *LWT - Food Science and Technology*. Academic Press, 64(2), pp. 750–758. doi: 10.1016/J.LWT.2015.06.051.

Stuetzer, O. M. (1960) 'Ion Drag Pumps', *Journal of Applied Physics*. American Institute of Physics, 31(1), pp. 136–146. doi: 10.1063/1.1735388.

TA, A. and MA., N. (1977) 'Drop formation characteristics of electrostatic ink jet using water-based ink', *IEEE Transactions on Electron Devices*, 24(3), pp. 262–6. Available at: https://ieeexplore.ieee.org/abstract/document/1478909/ (Accessed: 18 June 2019).

Tirumala, R. and Go, D. B. (2014) 'Comparative study of corona discharge simulation techniques for electrode configurations inducing non-uniform electric fields', *Journal of Electrostatics*. Elsevier Ltd, 72(2), pp. 99–106. doi: 10.1016/j.elstat.2013.12.003.

Velev, O. D. and Bhatt, K. H. (2006) 'On-chip micromanipulation and assembly of colloidal particles by electric fields', *Soft Matter*, 2(9), p. 738. doi: 10.1039/b605052b.

Wan, C. (2009) *Electro-hydrodynamic (EHD) thruster analisis and optimization*. Albert Nerken School of Engineering.

WAN, C. (2009) *ELECTRO-HYDRODYNAMIC (EHD) THRUSTER ANALYSIS AND OPTIMIZATION*. The Cooper Union for the Advancement of Science and Art.

Wegener, M. and Paschedag, A. R. (2011) 'Mass transfer enhancement at deformable droplets due to Marangoni convection', *International Journal of Multiphase Flow*. Pergamon, 37(1), pp. 76–83. doi: 10.1016/J.IJMULTIPHASEFLOW.2010.08.005.

Zeng, J. and Korsmeyer, T. (2004) 'Principles of droplet electrohydrodynamics for lab-on-a-chip', *Lab on a Chip*, 4(4), p. 265. doi: 10.1039/b403082f.

Zhao, L. and Adamiak, K. (2016) 'EHD flow produced by electric corona discharge in gases: From fundamental studies to applications (a review)', *Particulate Science and Technology*. 2016, 34(1), pp. 63–71. doi: 10.1080/02726351.2015.1043677.